NASA Technical Paper 3386

CECOM Technical Report 93-E-1

October 1993

Resonant Frequencies of Irregularly Shaped Microstrip Antennas Using Method of Moments

Manohar D. Deshpande,
David G. Shively,
and C. R. Cockrell

NASA

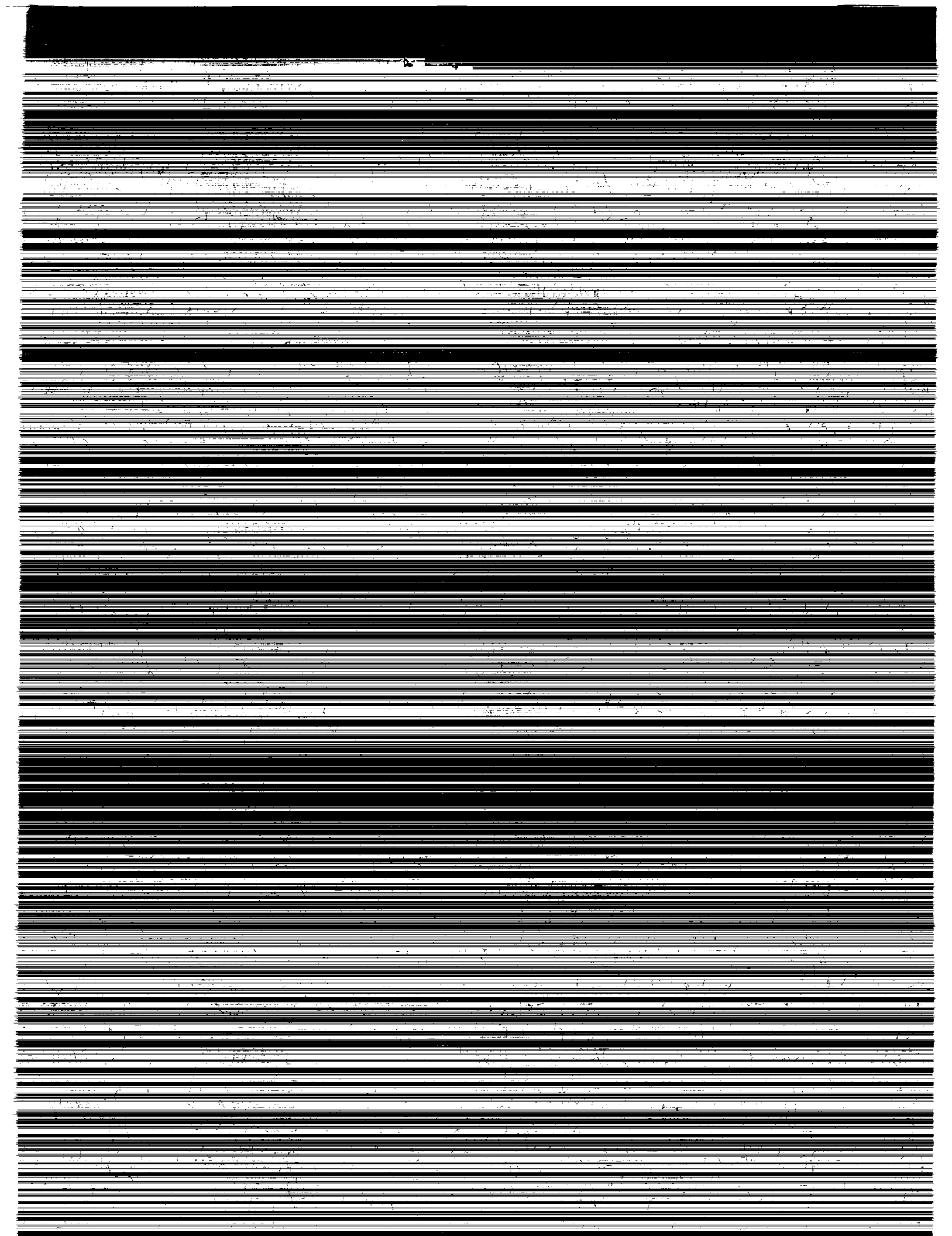

NASA Technical Paper 3386

CECOM Technical Report 93-E-1

1993

Resonant Frequencies of Irregularly Shaped Microstrip Antennas Using Method of Moments

Manohar D. Deshpande
ViGYAN, Inc.
Hampton, Virginia

David G. Shively
Joint Research Program Office
Electronics Integration Directorate
Communications Electronics Command
Langley Research Center
Hampton, Virginia

C. R. Cockrell
Langley Research Center
Hampton, Virginia

NASA
National Aeronautics and Space Administration
Office of Management
Scientific and Technical Information Program

Abstract

This paper describes an application of the method of moments to determine resonant frequencies of irregularly shaped microstrip patches embedded in a grounded dielectric slab. For analysis, the microstrip patch is assumed to be excited by a linearly polarized plane wave that is normal to the patch. The surface-current density that is induced on the patch because of the incident field is expressed in terms of subdomain functions by dividing the patch into identical rectangular subdomains. The amplitudes of the subdomain functions, as a function of frequency, are determined using the electric-field integral equation (EFIE) approach in conjunction with the method of moments. The resonant frequencies of the patch are then obtained by selecting the frequency at which the amplitude of the surface-current density is real. The resonant frequencies of the equilateral triangular and other nonrectangular patches are computed using the present technique, and these frequencies are compared with measurements and other independent calculations.

Introduction

Microstrip patch antennas have been studied extensively in recent years because they offer many practical advantages, such as being lightweight, able to conform to the body of a host object, and relatively easy and inexpensive to fabricate compared with other types of antennas. As a result, many analytical approaches have been proposed to analyze microstrip patch antennas (ref. 1). The electric-field integral equation (EFIE) approach in conjunction with the method of moments is the most widely used technique to study microstrip patch antennas (refs. 2 to 6). Early work (refs. 2 to 6) on the application of the EFIE approach to patches is limited to microstrip patches of regular shapes, such as those that are rectangular, circular, or elliptical. Furthermore, these earlier works (refs. 2 to 6) use an approach in which the surface-current density on the patch is expressed in terms of entire domain functions. This paper describes the EFIE approach in conjunction with the method of moments for solving the problem of irregularly shaped microstrip patch antennas by expressing the surface currents in terms of subdomain functions.

Several authors (refs. 7 and 8) have used the EFIE approach to analyze irregularly shaped antennas. The work in references 7 and 8, however, is applicable to irregular plates in free space. In these papers, a nonrectangular plate is viewed as an interconnection of quadrilateral plates. The currents on the quadrilateral plates are expressed in terms of nonrectangular surface modes. Although the segmentation techniques used in reference 7 completely fill the area of the nonrectangular plate, extra current modes are required to ensure continuity of surface-current density at the joining plates of the junctions. Furthermore, when nonrectangular surface modes are used to express the surface currents, the resulting matrix in the method of moments solution is of a symmetrical but not of a Toeplitz nature; therefore, the computational time increases.

Mosig (ref. 9) and Michalski and Zheng (ref. 10) use a mixed potential integral equation approach to solve the problem of irregularly shaped microstrip patches. In these studies, the EFIE is solved by using numerical techniques in the spatial domain which may require special care to handle the singularity in the Green's function. Martinson and Kuester (ref. 11) use generalized edge boundary conditions to accurately analyze irregularly shaped microstrip patches. This approach, however, is valid only for thin substrates (e.g., $d/\lambda_0 \leq 0.01$).

This work describes a segmentation technique to analyze irregularly shaped microstrip patch antennas. We assume that an irregularly shaped patch is enclosed by a rectangle with sides equal

to W_x and W_y. After dividing W_x into $(M+1)$ sections and W_y into $(N+1)$ sections, the surface-current density over the rectangle is expressed in terms of overlapping triangular functions in the current flow direction and pulse functions in the orthogonal direction. A shape function in the current expansion function is introduced to ensure zero current outside the patch. The shape function is equal to 1 if the subdomain lies inside the irregularly shaped patch antenna, and it is equal to 0 if the subdomain lies outside the irregularly shaped patch antenna. However, for the truly irregular shaped patch, the subdomain that is close to the boundaries of the patch may be partly occupied by the patch. In such cases, the subdomain is considered to be inside the patch if the area occupied by the patch in that subdomain is more than 50 percent of the area of the subdomain. This process of finding the shape function, however, becomes tedious and time consuming for complicated geometries.

The EFIE equation is reduced to a matrix equation that is solved using standard matrix equation solver subroutines when the testing functions are selected to be the same as the expansion functions (i.e., a Galerkin solution). The surface-current density is then used to determine the resonant frequency of the patch. One of the disadvantages of the present method is that a large number of subdomains are required to achieve convergence because the edge conditions for the surface-current distributions are not explicity expressed. However, the Toeplitz nature of the impedance matrix is still maintained, thus considerably reducing the matrix filling time (ref. 12).

Symbols

$\hat{\mathbf{a}}_x, \hat{\mathbf{a}}_y, \hat{\mathbf{a}}_z$	unit vectors along x, y, and z axes
d	dielectric substrate thickness, cm
$\mathbf{E}_i$	incident electric-field vector
E_{i0}	intensity of incident electric field
$\mathbf{E}_s(J_x)$	scattered electric-field vector caused by J_x
$\mathbf{E}_s(J_y)$	scattered electric-field vector caused by J_y
$\mathbf{E}_{ti}$	tangential electric-field vector
E_{xi}, E_{yi}	x and y components of incident electric field
$E_{xs}(J_x)$	x component of scattered electric-field caused by J_x
$E_{xs}(J_y)$	x component of scattered electric field caused by J_y
$E_{ys}(J_x)$	y component of scattered electric field caused by J_x
$E_{ys}(J_y)$	y component of scattered electric field caused by J_y
E_{10}	electric-field amplitude for perpendicular polarization, V/m
E_{20}	electric-field amplitude for parallel polarization, V/m
$F_{xmn}(x, y)$	expansion function for x-directed current on (m, n)th subdomain
$F_{xp}(x, y)$	expansion function for x-directed current on pth subdomain
$F_{ymn}(x, y)$	expansion function for y-directed current on (m, n)th subdomain
$F_{yp}(x, y)$	expansion function for y-directed current on pth subdomain
$f_{0,\ldots,5}$	resonant frequencies of various modes, GHz
$f_{xp'}$	Fourier transform of $F_{xp'}(x, y)$
$f_{yp'}$	Fourier transform of $F_{yp'}(x, y)$

$\mathbf{H}_i$	incident magnetic field vector
$i_x(m,n)$	complex amplitude of x-directed current density on (m,n)th subdomain, A/unit area
$i_y(m,n)$	complex amplitude of y-directed current density on (m,n)th subdomain, A/unit area
$i_x(p)$	complex amplitude of x-directed current density on pth subdomain, A/unit area
$i_y(p)$	complex amplitude of y-directed current density on pth subdomain, A/unit area
$J_x(x,y)$	x-directed induced surface-current density on plate, A/unit area
$J_y(x,y)$	y-directed induced surface-current density on plate, A/unit area
j	$=\sqrt{-1}$
k_0	propagation constant/wave number in free space
$\mathbf{k}_i$	propagation vector of plane wave
$M+1$	number of subdivisions in x-direction
m,n	(m,n)th subdomain of induced current
$N+1$	number of subdivisions in y direction
P	total number of x-directed subdomains on plate
$P_m(x)$	piecewise linear distribution in x-direction
$P_n(y)$	piecewise linear distribution in y-direction
p	equivalent to (m,n)th x-directed subdomain
p'	equivalent to (m',n')th x-directed subdomain
Q	total number of y-directed subdomains on plate
$Q_m(y)$	pulse distribution in y-direction
$Q_n(x)$	pulse distribution in x-direction
$\mathbf{r}$	position vector in direction of plane wave
$v_x(p')$	reaction of p'th x-directed subdomain testing function with E_{xi}
$v_y(p')$	reaction of p'th y-directed subdomain testing function with E_{yi}
W_x	maximum dimension of plate in x-direction, cm
W_y	maximum dimension of plate in y-direction, cm
x,y,z	Cartesian coordinates of field point
x',y',z'	Cartesian coordinates of source point
x_m	$=m\,\Delta x$
Z'	location of patch, cm
$Z_{xx}^{p,p'}$	mutual impedance between pth and p'th x-directed subdomain currents, ohm
$Z_{xy}^{p,p'}$	mutual impedance between pth y-directed and p'th x-directed subdomain currents, ohm

$Z_{yx}^{p,p'}$	mutual impedance between pth x-directed and p'th y-directed subdomain currents, ohm
$Z_{yy}^{p,p'}$	mutual impedance between pth and p'th y-directed subdomain currents, ohm
α	wedge angle, deg
Δx	$= \frac{W_x}{M+1}$
Δy	$= \frac{W_y}{N+1}$
ε_r	relative dielectric constant of slab material
η_0	free-space wave impedance, ohm
θ_i, ϕ_i	direction of angle of incident wave, deg
λ_0	wavelength in free space, cm

Abbreviation:

TM	transverse magnetic

Theory

General Theory

Consider an irregularly shaped thin patch embedded in a dielectric slab and illuminated by a plane wave as shown in figure 1. The incident field can be expressed as

$$\mathbf{E}_i(x,y,z) = E_{i0}\left[-\hat{\mathbf{a}}_x \sin(\phi_i) + \hat{\mathbf{a}}_y \cos(\phi_i)\right] \exp\left[(jk_0\mathbf{k}_i)\cdot\mathbf{r}\right] \tag{1}$$

for perpendicular polarization, and

$$\mathbf{H}_i(x,y,z) = \frac{E_{i0}}{\eta_0}\left[-\hat{\mathbf{a}}_x \sin(\phi_i) + \hat{\mathbf{a}}_y \cos(\phi_i)\right] \exp\left[(jk_0\mathbf{k}_i)\cdot\mathbf{r}\right] \tag{2}$$

for parallel polarization, where η_0 and k_0 are the free-space wave impedance and the wave number, respectively, and (θ_i, ϕ_i) is the direction of the angle of incident wave. In equations (1) and (2), E_{i0} is the incident electric-field intensity; the quantities $\hat{\mathbf{a}}_x$, $\hat{\mathbf{a}}_y$, and $\hat{\mathbf{a}}_z$ are the unit vectors along the x, y, and z axes, respectively; and

$$\mathbf{k}_i = \hat{\mathbf{a}}_x \sin(\theta_i)\cos(\phi_i) + \hat{\mathbf{a}}_y \sin(\theta_i)\sin(\phi_i) + \hat{\mathbf{a}}_z \cos(\theta_i)$$

$$\mathbf{r} = \hat{\mathbf{a}}_x x + \hat{\mathbf{a}}_y y + \hat{\mathbf{a}}_z z$$

The tangential electric field in the plane of the patch when the patch is absent (ref. 12) is then obtained as

$$\mathbf{E}_{ti} = E_{10}\left[-\hat{\mathbf{a}}_x \sin(\phi_i) + \hat{\mathbf{a}}_y \cos(\phi_i)\right] \exp\left\{j\left[(k_0\mathbf{k}_i)\cdot\hat{\mathbf{a}}_x\right]x\right\} + \left\{j\left[(k_0\mathbf{k}_i)\cdot\hat{\mathbf{a}}_y\right]y\right\} \tag{3}$$

for perpendicular polarization, and

$$\mathbf{E}_{ti} = E_{20}\left[-\hat{\mathbf{a}}_x \cos(\phi_i) + \hat{\mathbf{a}}_y \sin(\phi_i)\right] \exp\left\{j\left[(k_0\mathbf{k}_i)\cdot\hat{\mathbf{a}}_x\right]x\right\} + \left\{j\left[(k_0\mathbf{k}_i)\cdot\hat{\mathbf{a}}_y\right]y\right\} \tag{4}$$

for parallel polarization, where

$$E_{10} = \frac{j\,2E_{i0}\cos(\theta_i)\sin(k_0 z' k_z)}{k_z\cos(k_0 d k_z) + j\cos(\theta_i)\sin(k_0 d k_z)} \exp\left[jk_0 d\cos(\theta_i)\right]$$

$$E_{20} = \frac{-j\,2E_{i0}\,k_z\cos(\theta_i)\sin(k_0 z' k_z)}{\varepsilon_r\cos(\theta_i)\cos(k_0 d k_z) + j k_z \sin(k_0 d k_z)} \exp\left[j k_0 d \cos(\theta_i)\right]$$

and $k_z = \sqrt{\varepsilon_r - \sin^2(\theta_i)}$.

Let $J_x(x', y')$ and $J_y(x', y')$ be the x- and y-directed induced electric surface-current densities on the patch and $\mathbf{E}_s(J_x)$ and $\mathbf{E}_s(J_y)$ be the scattered electric fields caused by the x- and y-directed currents, respectively. Setting the total tangential electric field over the patch to zero yields

$$\hat{\mathbf{a}}_z \times \left[\mathbf{E}_s\left(J_x\right) + \mathbf{E}_s\left(J_y\right) + \mathbf{E}_i\right] = 0 \tag{5a}$$

Equation (5a) can be written in component form as

$$\left.\begin{aligned} E_{xs}\left(J_x\right) + E_{xs}\left(J_y\right) + E_{xi} = 0 \\ E_{ys}\left(J_x\right) + E_{ys}\left(J_y\right) + E_{yi} = 0 \end{aligned}\right\} \tag{5b}$$

where the suffixes x and y are used to indicate the x and y components of the scattered and incident fields. To solve equations (5) for $J_x(x', y')$ and $J_y(x', y')$, the x- and y-directed currents on the patch are expressed as

$$J_x\left(x', y'\right) = \sum_{m=1}^{M}\sum_{n=1}^{N+1} i_x(m,n)\, F_{xmn}\left(x', y'\right) \tag{6a}$$

$$J_y\left(x', y'\right) = \sum_{m=1}^{M+1}\sum_{n=1}^{N} i_y(m,n)\, F_{ymn}\left(x', y'\right) \tag{6b}$$

In deriving equations (6), the irregularly shaped patch is first enclosed by a rectangle with sides W_x and W_y, and this rectangle is then divided into $M+1$ and $N+1$ sections along the x and y directions, respectively, as shown in figure 1(b). The quantities $i_x(m,n)$ and $i_y(m,n)$ in equations (6) are the amplitudes of surface-current densities at the (m,n)th subdomain. The expansion functions $F_{xmn}(x', y')$ and $F_{ymn}(x', y')$ in equations (6) are given by

$$F_{xmn}\left(x', y'\right) = P_m\left(x'\right) Q_n\left(y'\right)$$

$$F_{ymn}\left(x', y'\right) = Q_m\left(x'\right) P_n\left(y'\right)$$

where

$$P_m\left(x'\right) = \begin{cases} 1 - \frac{x_m - x'}{\Delta x} & \left((x_m - \Delta x) \le x' \le x_m\right) \\ 1 - \frac{x' - x_m}{\Delta x} & \left(x_m \le x' \le (x_m - \Delta x)\right) \end{cases}$$

$$Q_n\left(y'\right) = \begin{cases} 1 & \left((n-1)\,\Delta y \le y' \le n\,\Delta y\right) \\ 0 & \text{(Otherwise)} \end{cases}$$

$$\Delta x = \frac{W_x}{M+1}$$

$$\Delta y = \frac{W_y}{N+1}$$

In the above expressions, $P_n(y')$ is obtained by replacing m and x' in the expression for $P_m(x')$ by n and y', respectively. Similarly, $Q_m(x')$ is obtained by replacing n and y' in the expression for $Q_n(y')$ by m and x', respectively. For simplicity, the double summation with respect to m and n in equations (6) can be represented by a single summation with respect to p. If P and Q are

the maximum numbers of the x- and y-directed subdomain cells, respectively, on the patch, then equations (6) may be rewritten as

$$\left.\begin{aligned} J_x(x',y') &= \sum_{p=1}^{P} i_x(p)\, F_{xp}(x',y') \\ J_y(x',y') &= \sum_{p=P+1}^{P+Q} i_y(p)\, F_{yp}(x',y') \end{aligned}\right\} \tag{7}$$

Using the method of moments and test modes that are identical to expansion modes, equations (5) yield

$$\iint E_{xs}(J_x)\, F_{xp'}(x,y)\, dx\, dy + \iint E_{xs}(J_y)\, F_{xp'}(x,y)\, dx\, dy + \iint E_{xi} F_{xp'}(x,y)\, dx\, dy = 0 \tag{8a}$$

where $p' = 1, 2, 3, \ldots, P$, and

$$\iint E_{ys}(J_x)\, F_{yp'}(x,y)\, dx\, dy + \iint E_{ys}(J_y)\, F_{yp'}(x,y)\, dx\, dy + \iint E_{xi} F_{yp'}(x,y)\, dx\, dy = 0 \tag{8b}$$

where $p' = P+1, P+2, P+3, \ldots, P+Q$, the surface integrals in equations (8a) and (8b) are carried out over the p' subdomain. Equations (8a) and (8b) can be written in the following convenient matrix form:

$$\begin{bmatrix} Z_{xx}^{p,p'} & Z_{xy}^{p,p'} \\ Z_{yx}^{p,p'} & Z_{yy}^{p,p'} \end{bmatrix} \begin{bmatrix} i_x(p) \\ i_y(p) \end{bmatrix} = \begin{bmatrix} v_x(p') \\ v_y(p') \end{bmatrix} \tag{9}$$

where $p' = 1, 2, 3, \ldots, (P+Q)$ and $Z_{xx}^{p,p'}$ and $Z_{xy}^{p,p'}$ are the self and mutual impedances between pth and p'th current basis functions. Detailed expressions for these impedances are given in reference 5. The elements of excitation vectors in equation (9) are given by

$$v_x(p') = -E_{10} \sin(\phi_i)\, f_{xp'}\left[(k_0 \mathbf{k}_i \cdot \hat{\mathbf{a}}_x), (k_0 \mathbf{k}_i \cdot \hat{\mathbf{a}}_y)\right] \tag{10}$$

$$v_y(p') = E_{10} \cos(\phi_i)\, f_{yp'}\left[(k_0 \mathbf{k}_i \cdot \hat{\mathbf{a}}_x), (k_0 \mathbf{k}_i \cdot \hat{\mathbf{a}}_y)\right] \tag{11}$$

for perpendicular polarization, and

$$v_x(p') = E_{20} \cos(\phi_i)\, f_{xp'}\left[(k_0 \mathbf{k}_i \cdot \hat{\mathbf{a}}_x), (k_0 \mathbf{k}_i \cdot \hat{\mathbf{a}}_y)\right] \tag{12}$$

$$v_y(p') = E_{20} \sin(\phi_i)\, f_{yp'}\left[(k_0 \mathbf{k}_i \cdot \hat{\mathbf{a}}_x), (k_0 \mathbf{k}_i \cdot \hat{\mathbf{a}}_y)\right] \tag{13}$$

for parallel polarization, where $f_{xp'}$ and $f_{yp'}$ are the Fourier transforms of $F_{xp'}$ and $F_{yp'}$, respectively.

Resonant Frequency

The current density that is excited by an incident plane wave is obtained by solving the matrix equation (9). The current amplitudes $i_x(p)$ and $i_y(p)$ are in general complex quantities; however, at resonance, $i_x(p)$ and $i_y(p)$ are real numbers. The resonant frequency of the patch may therefore be defined as a frequency at which the real part of $i_x(p)$ and $i_y(p)$ is maximum and the imaginary part is zero. The dominant and higher order resonances of an irregularly shaped patch can therefore be determined by finding the frequencies at which the real part of the surface-current density is maximum and the imaginary part of the surface-current density is zero.

Numerical Results

In this section, resonant frequencies of irregularly shaped patch antennas are obtained and compared with the measured data and the results obtained using the cavity model (refs. 13 and 14).

The induced currents $i_x(p)$ and $i_y(p)$ are determined using equation (9) as a function of frequency. The dominant and higher order resonances of the patch are determined from the knowledge of the variation of $i_x(p)$ and $i_y(p)$ as a function of frequency.

Resonant Frequencies of Equilateral Triangular Patch

As a first example, we select an equilateral triangular patch with dimensions $a = 10$ cm, $\varepsilon_r = 2.32$, and $d = z' = 0.16$ cm, as shown in figure 2. For resonant frequency calculations, the patch is assumed to be excited by a parallel polarized plane wave at normal incidence with $\phi_i = 0°$ or $\phi_i = 90°$.

The triangular patch is assumed to be enclosed by a rectangle with $W_x = 10$ cm and $W_y = 8.66$ cm, as shown in figure 2. Selecting values of M and N (e.g., $M = N = 11$) and defining the (m, n)th subdomain for the x- and y-directed currents to be inside the triangular patch if more than 50 percent of the subdomain area lies inside the patch, the matrix equation (9) is solved for $i_x(p)$ and $i_y(p)$. The current densities $i_x(p)$ and $i_y(p)$ that are normalized to the incident field at the center of the patch are then plotted in figures 3(a) and 3(b) for the two incidence angles ($\theta_i = 0°$, $\phi_i = 90°$) and ($\theta_i = 0°$, $\phi_i = 0°$), respectively. From figures 3(a) and 3(b), we see that the resonant frequencies at which the real part of the current density is maximum and the imaginary part of the current density crosses zero are $f_0 = 1.210$ GHz and $f_1 = 1.256$ GHz.

To test the dependence of these resonant frequencies on M and N, the resonant frequencies are calculated as a function of M and N and are plotted in figure 4. This figure clearly shows that $M = N \geq 19$ gives stable numerical results and that the first resonance occurs at $f_0 = 1.249$ GHz and the second resonance occurs at $f_1 = 1.276$ GHz.

Microstrip patch resonances are usually associated with the cavity modes described in reference 14. To identify the above two resonances with cavity modes, we must plot a vectorial representation of the surface-current density over the patch that is excited by an incident plane wave at resonant frequencies $f_0 = 1.249$ GHz and $f_1 = 1.276$ GHz, as is done in figures 5(a) and 5(b). These figures show that the magnitude of the surface-current density is proportional to the length of the vector, while the direction of the current flow is indicated by the arrow direction. Upon careful examination of the resonances of the TM_{01} (transverse magnetic) and TM_{10} cavity modes given in reference 14, it is clear that the resonance at $f_0 = 1.249$ GHz corresponds to the TM_{01} mode, and that the resonance at $f_1 = 1.276$ GHz corresponds to the TM_{10} cavity mode. Note that the cavity model discussed in references 13 and 14 predicts that the resonant frequencies of the TM_{10} and TM_{01} modes are identical. This technique, however, gives slightly different resonant frequencies of these modes; this difference may be attributed to discretization of the patch.

To study higher order resonances of the triangular patch, surface-current densities that are excited by plane waves for the incident angles of ($\theta_i = 0°$, $\phi_i = 0°$) and ($\theta_i = 0°$, $\phi_i = 90°$) are plotted in figures 6 and 7, respectively, over a wider frequency band. The resonant frequencies of higher order modes of the patch are determined from these figures, and they are presented in table 1 with the corresponding cavity modes calculated using the cavity model (ref. 14) and measured results given in reference 13.

The resonant frequencies of the TM_{mn} and TM_{nm} modes are identical, as seen from the cavity model formulations. As noted earlier, the present method that is based on discretization predicts the resonant frequencies of these modes to be slightly different from each other. Corresponding vectorial representations of the surface-current densities at incident angles of ($\theta_i = 0°$, $\phi_i = 0°$) and ($\theta_i = 0°$, $\phi_i = 90°$) are depicted in figures 8 and 9, respectively, for higher order resonant frequencies.

Resonant Frequencies of Circular Patch

As a second example, we consider a circular patch with a = 1.88 cm, as shown in figure 10. This patch is assumed to be excited by a parallel polarized plane wave at normal incidence with $\phi_i = 0°$

or $\phi_i = 90°$. The induced current density $i_x(p)$ and $i_y(p)$ as a function of frequency at the center of the patch is obtained after solving equation (9), and it is plotted in figures 11(a) and 11(b). Values of M and N were arbitrarily selected to be $M = N = 11$. These figures show that the frequency at which the real parts of the current densities are maximum and the imaginary parts of the current densities are zero is $f_0 = 2.760$ GHz. The first resonance of the patch is therefore at 2.760 GHz. To test the dependence of the first resonance on M and N, f_0 is determined as a function of M and N, and it is plotted in figure 12. Figure 12 clearly shows that $M = N \geq 19$ gives stable numerical results. This figure also gives the first resonant frequency of the circular patch obtained using the method described in reference 15. Good agreement exists between the two results for $M = N \geq 19$. The vectorial representations of the surface-current density over the circular patch, excited by the x- and y-directed linearly polarized plane waves at the first resonant frequency, are shown in figures 13(a) and 13(b), respectively. Comparison of this representation with the cavity model representation (ref. 14) indicates that the resonant mode at a frequency of 2.760 GHz corresponds to the TM_{11} cavity mode.

Higher order resonances of the circular patch are determined, and they are given in table 2. This table also gives higher order resonances that are calculated using the cavity model (ref. 14). Good agreement exists between the two methods. A vectorial representation of the surface-current densities at higher order resonant frequencies is given in figure 14. A comparison of these representations with the representations obtained by the cavity model confirms that resonances at frequencies of 4.685 GHz, 5.855 GHz, and 6.360 GHz correspond to the TM_{21}, TM_{02}, and TM_{31} cavity modes (ref. 14).

Resonant Frequency of Trapezoidal Patch

As a third example, we consider a trapezoidal patch with dimensions as shown in figure 15. Figures 16(a) and 16(b) present the variation of current density as a function of frequency at the center of the trapezoidal patch for two angles of incidence. These plots show that the frequency at which the real part of the current density is maximum while the imaginary part is zero is 1.342 GHz. The first resonance of the patch therefore occurs at a frequency of 1.342 GHz. To test the dependence of the first resonance on M and N, the first resonance frequency of the patch is calculated as a function of M and N, and it is given in table 3. Table 3 clearly shows that $M \geq 12$ and $N \geq 6$ give stable numerical results. Figure 17 gives the vectorial representation of the surface-current density on the patch at the first resonance for incident angle of ($\theta_i = 0°$, $\phi_i = 0°$).

Conclusions

An electric-field integral equation approach in conjunction with the method of moments has been used to determine the resonant frequencies of irregularly shaped microstrip patches. Numerical results obtained using this approach compare well with experimental results and other independent calculations. Discretization of an irregular patch into symmetrical rectangular subdomains, in the present technique, results in a symmetrical and block Toeplitz impedance matrix. The discretization scheme used, however, does not explicitly enforce the proper edge conditions on the surface-current distribution. As a result, a large number of subdomains are required to achieve numerical convergence.

NASA Langley Research Center
Hampton, VA 23681-0001
August 16, 1993

References

1. Carver, Keith R.; and Mink, James W.: Microstrip Antenna Technology. *IEEE Trans. Antennas & Propag.*, vol. AP-29, no. 1, Jan. 1981, pp. 2–24.

2. Newman, Edward H.; and Tulyathan, Pravit: Analysis of Microstrip Antennas Using Moment Methods. *IEEE Trans. Antennas & Propag.*, vol. AP-29, no. 1, Jan. 1981, pp. 47–53.

3. Newman, Edward H.; and Forrai, David: Scattering From a Microstrip Patch. *IEEE Trans. Antennas & Propag.*, vol. AP-35, no. 3, Mar. 1987, pp. 245–251.

4. Pozar, David M.: Input Impedance and Mutual Coupling of Rectangular Microstrip Antennas. *IEEE Trans. Antennas & Propag.*, vol. AP-30, no. 6, Nov. 1982, pp. 1191–1196.

5. Bailey, M. C.; and Deshpande, M. D.: Integral Equation Formulation of Microstrip Antennas. *IEEE Trans. Antennas & Propag.*, vol. AP-30, no. 4, July 1982, pp. 651–656.

6. Bailey, M. C.; and Deshpande, M. D.: Analysis of Elliptical and Circular Microstrip Antennas Using Moment Method. *IEEE Trans. Antennas & Propag.*, vol. AP-33, no. 11, Sept. 1985, pp. 954–959.

7. Newman, Edward H.; and Tulyathan, Pravit: A Surface Patch Model for Polygonal Plates. *IEEE Trans. Antennas & Propag.*, vol. AP-30, no. 4, July 1982, pp. 588–593.

8. Singh, J.; and Adams, A. T.: A Nonrectangular Patch Model for Scattering From Surfaces. *IEEE Trans. Antennas & Propag.*, vol. AP-27, July 1979, pp. 531–535.

9. Mosig, Juan R.: Arbitrarily Shaped Microstrip Structures and Their Analysis With a Mixed Potential Integral Equation. *IEEE Trans. Microw. Theory & Tech.*, vol. 36, no. 2, Feb. 1988, pp. 314–323.

10. Michalski, Krzysztof A.; and Zheng, Dalian: Analysis of Microstrip Resonators of Arbitrary Shape. *IEEE Trans. Microw. Theory & Tech.*, vol. 40, no. 1, Jan. 1992, pp. 112–119.

11. Martinson, Thomas M.; and Kuester, Edward F.: Accurate Analysis of Arbitrarily Shaped Patch Resonators on Thin Substrates. *IEEE Trans. Microw. Theory & Tech.*, vol. 36, no. 2, Feb. 1988, pp. 324–331.

12. Deshpande, Manohar D.; Cockrell, C. R.; Beck, Fred B.; Vedeler, Erik; and Koch, Melissa B.: *Analysis of Electromagnetic Scattering From Irregularly Shaped, Thin, Metallic Flat Plates.* NASA TP-3361, 1993.

13. Lee, Kai-Fong; Luk, Kwai-Man; and Dahele, Jashwant S.: Characteristics of the Equilateral Triangular Patch Antenna. *IEEE Trans. Antennas & Propag.*, vol. 36, no. 11, Nov. 1988, pp. 1510–1518.

14. Bahl, I. J.; and Bhartia, P.: *Microstrip Antennas.* Artech House, Inc., c.1980.

15. Chew, W. C.; and Kong, J. A.: Analysis of a Circular Microstrip Disk Antenna With a Thick Dielectric Substrate. *IEEE Trans. Antennas & Propag.*, vol. AP-29, no. 1, Jan. 1981, pp. 68–76.

Table 1. Calculated and Measured Resonant Frequencies of Equilateral Triangular Patch for $M = N = 19$

[Patch shown in fig. 2]

Mode	Resonant frequency, GHz		
	Present method	Measured results (ref. 12)	Cavity model (ref. 13)
TM_{01}	1.249	1.280	1.299
TM_{10}	1.276		
TM_{11}	2.172	2.242	2.252
TM_{02}	2.525	2.550	2.599
TM_{20}	2.510		
TM_{12}	3.265		
TM_{21}	3.356	3.400	3.439

Table 2. Calculated Resonant Frequencies of Higher Order Modes of Circular Patch

[Patch shown in fig. 10]

Mode	Resonant frequency, GHz	
	Present method	Cavity model (ref. 13)
TM_{11}	2.816	2.818
TM_{21}	4.685	4.674
TM_{02}	5.855	5.864

Table 3. Resonant Frequencies of Trapezoidal Patch for Various Values of M and N

[Patch shown in fig. 15]

M	N	Resonant frequency, GHz
7	5	1.370
12	6	1.345
14	7	1.342
16	8	1.343
18	9	1.343
20	10	1.342

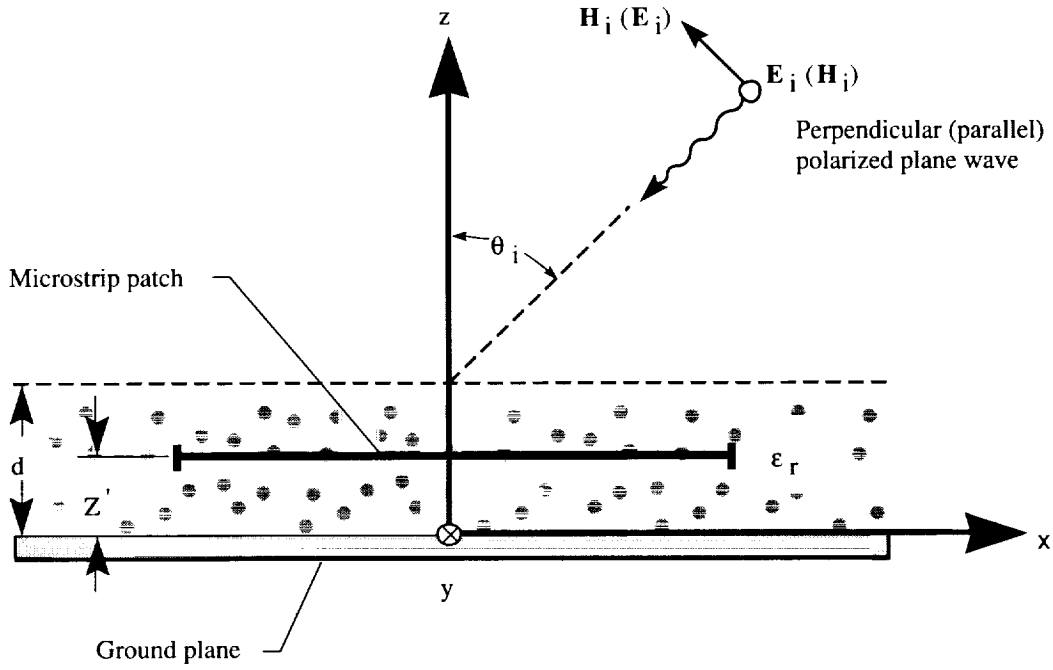

(a) Side view of microstrip antenna.

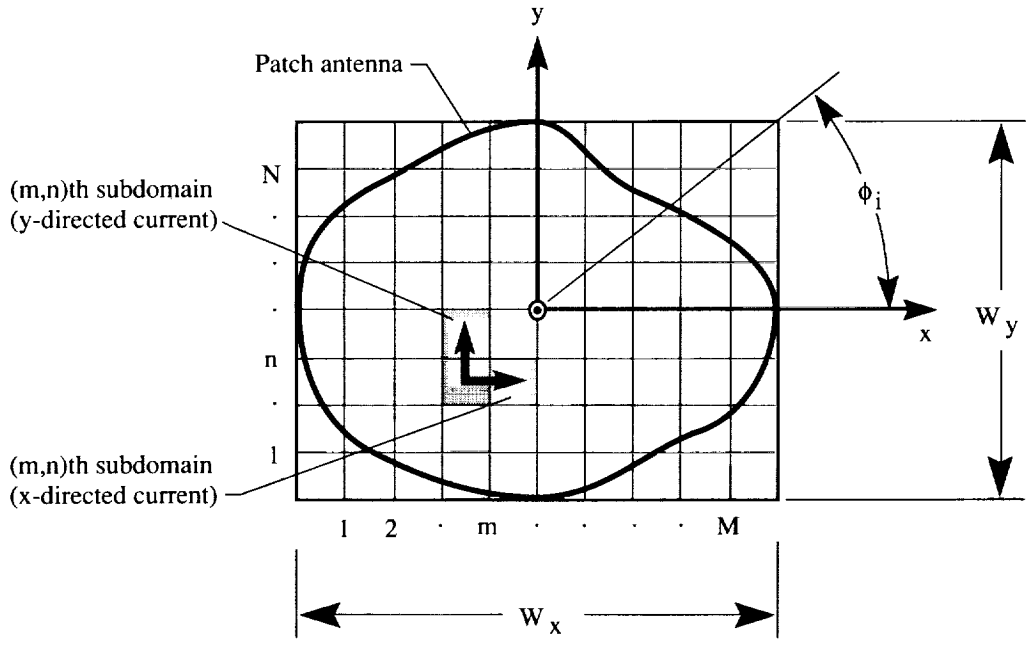

(b) Top view of microstrip antenna.

Figure 1. Geometry of microstrip antenna.

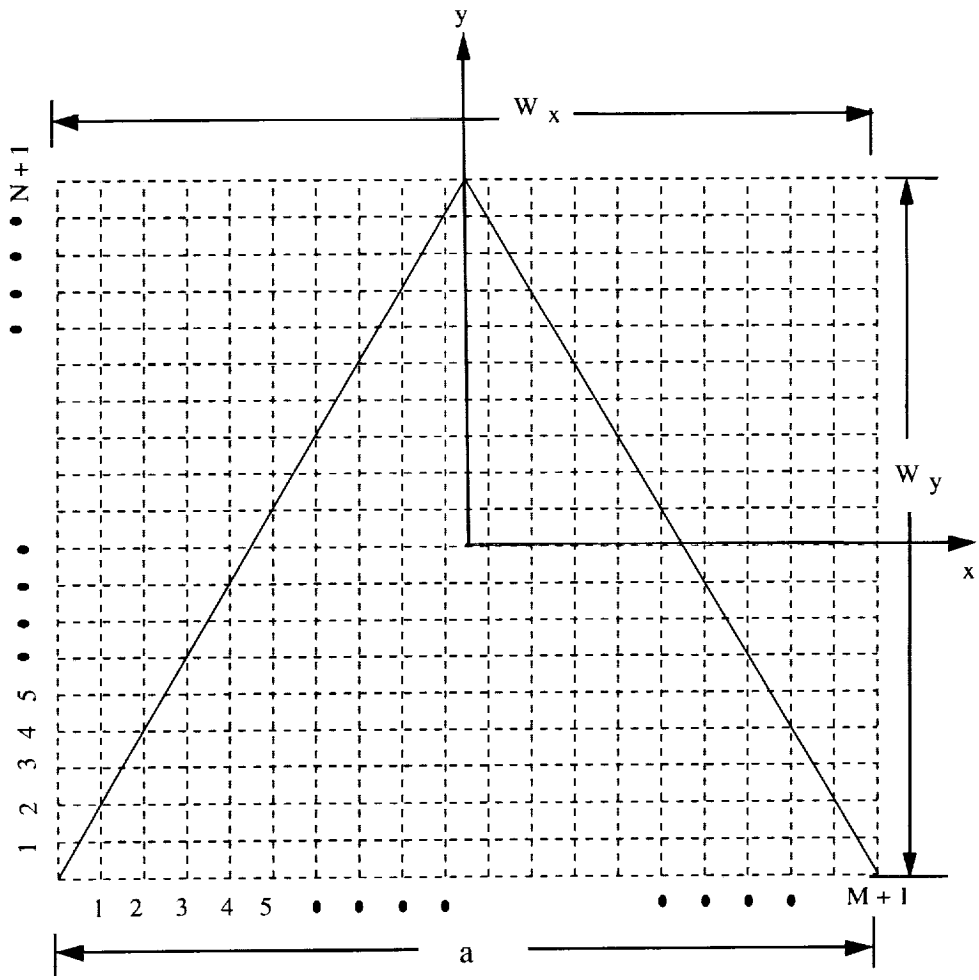

Figure 2. Geometry of equilateral triangular patch with dimensions a = 10 cm, $d = z' = 0.16$ cm, $\varepsilon_r = 2.32$, and loss tangent = 0.002.

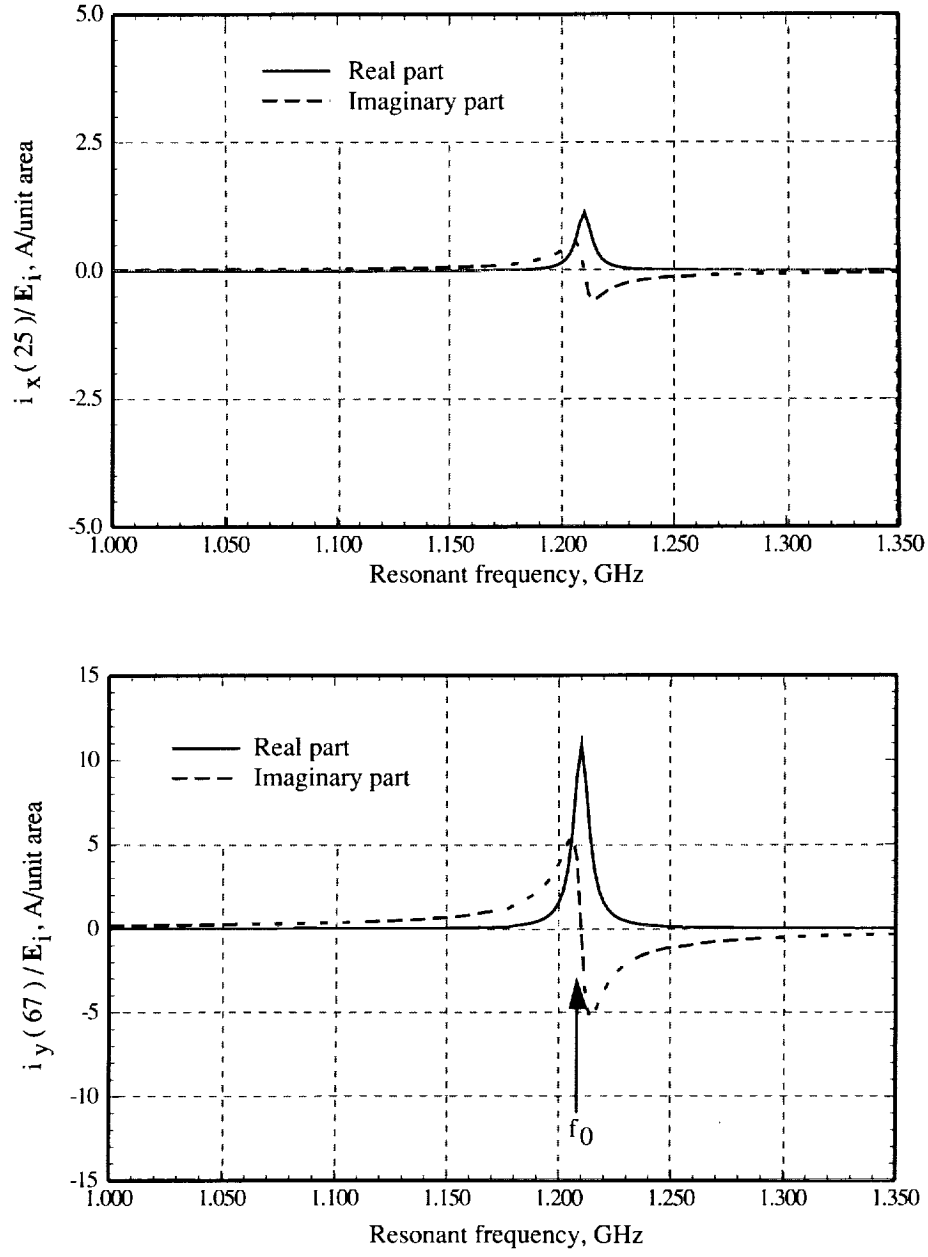

(a) $(\theta_i = 0°,\ \phi_i = 90°)$; $f_0 = 1.210$ GHz.

Figure 3. Normalized current density as function of resonant frequency for equilateral triangular patch (shown in fig. 2) for angles of incidence of $(\theta_i = 0°,\ \phi_i = 90°)$ and $(\theta_i = 0°,\ \phi_i = 0°)$, $M = N = 11$, $f_0 = 1.210$ GHz, and $f_1 = 1.256$ GHz.

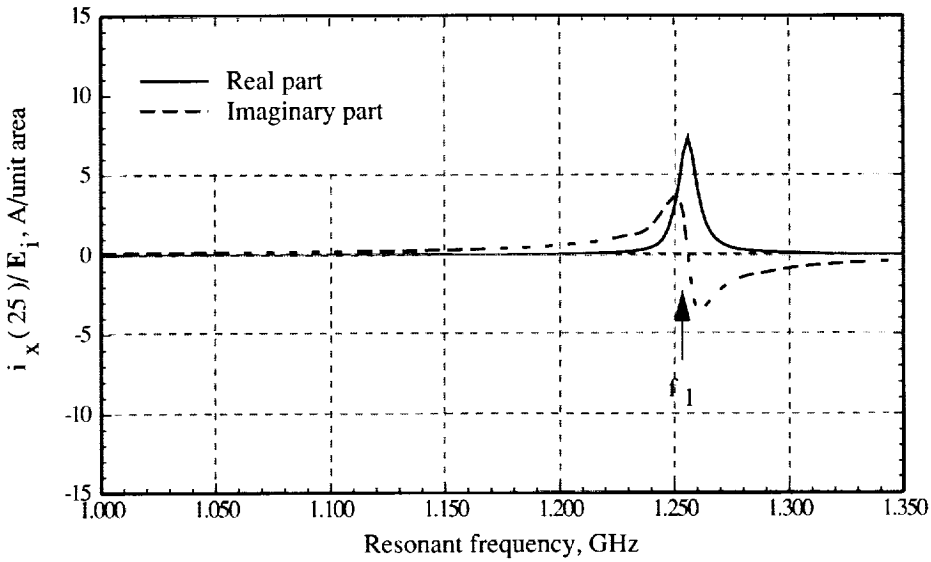

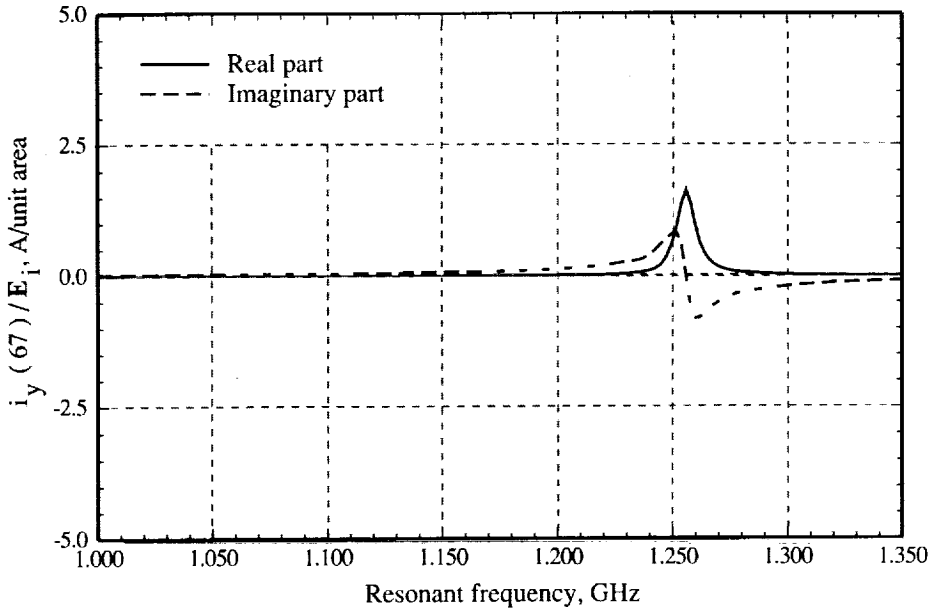

(b) $(\theta_i = 0°, \phi_i = 0°)$; $f_1 = 1.256$ GHz.

Figure 3. Concluded.

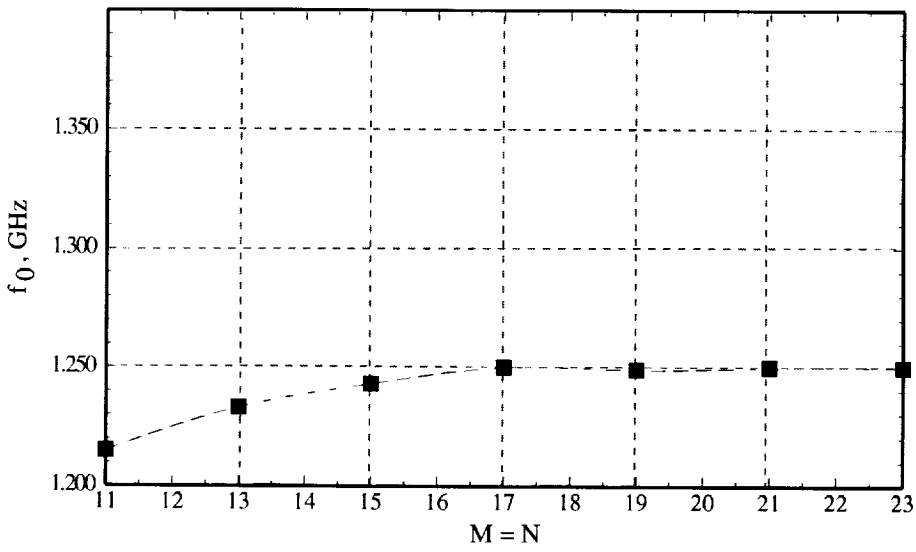

(a) Variation of f_0.

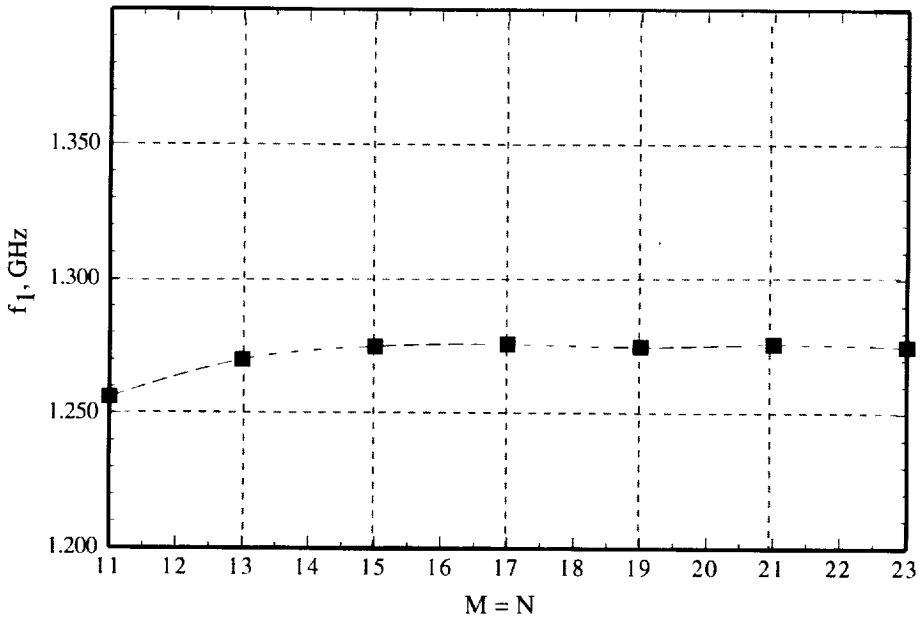

(b) Variation of f_1.

Figure 4. First two resonant frequencies of equilateral triangular patch (shown in fig. 2) for $M = N$.

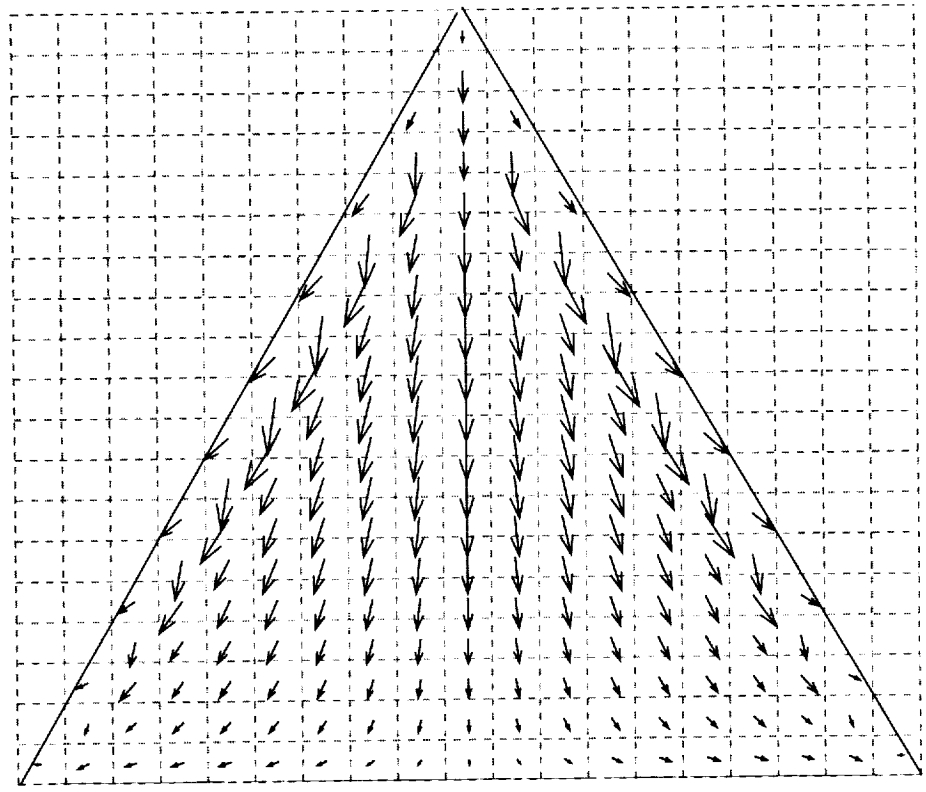

(a) $(\theta_i = 0°, \phi_i = 90°)$; $f_0 = 1.249$ GHz (TM_{01} mode case).

Figure 5. Vectorial representation of surface-current density on equilateral triangular patch (shown in fig. 2) excited by plane wave with angles of incidence of $(\theta_i = 0°, \phi_i = 90°)$ and $(\theta_i = 0°, \phi_i = 0°)$, $f_0 = 1.249$ GHz (TM_{01} mode case), and $f_1 = 1.276$ GHz (TM_{10} mode case).

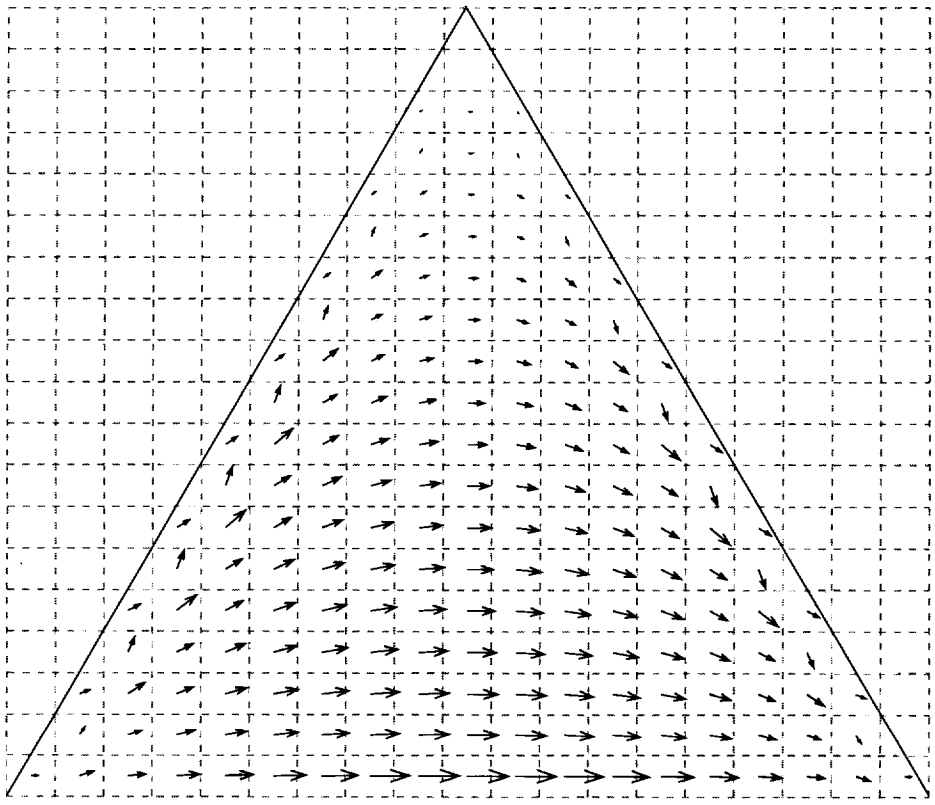

(b) $(\theta_i = 0°, \phi_i = 0°)$; $f_1 = 1.276$ GHz (TM_{10} mode case).

Figure 5. Concluded.

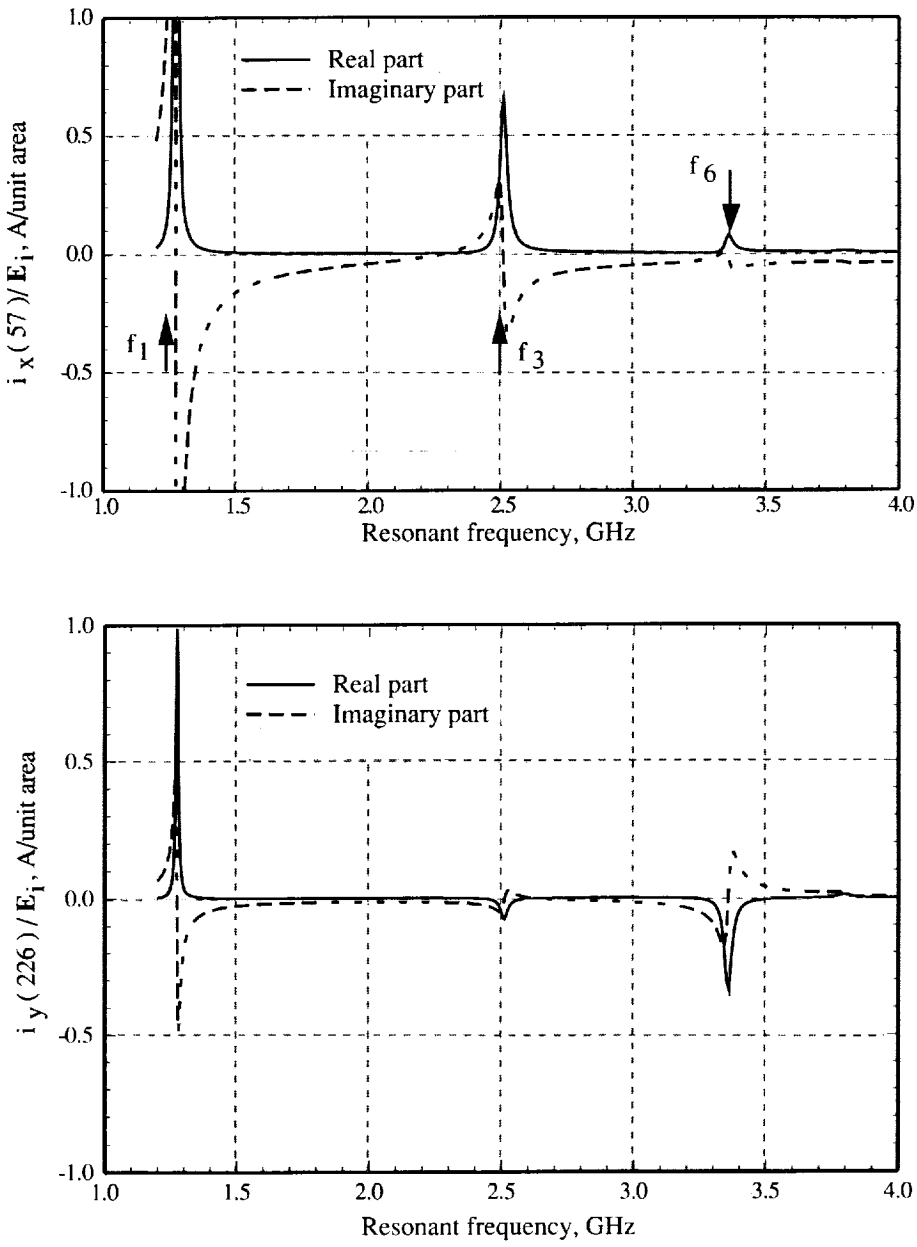

Figure 6. Normalized current density as function of resonant frequency for equilateral triangular patch (shown in fig. 2) excited by plane wave at angle of incidence of ($\theta_i = 0°$, $\phi_i = 0°$) and $M = N = 19$. The terms f_1 (1.276 GHz), f_3 (2.510 GHz), and f_6 (3.355 GHz) are resonant frequencies of TM_{10}, TM_{20}, and TM_{21} modes, respectively.

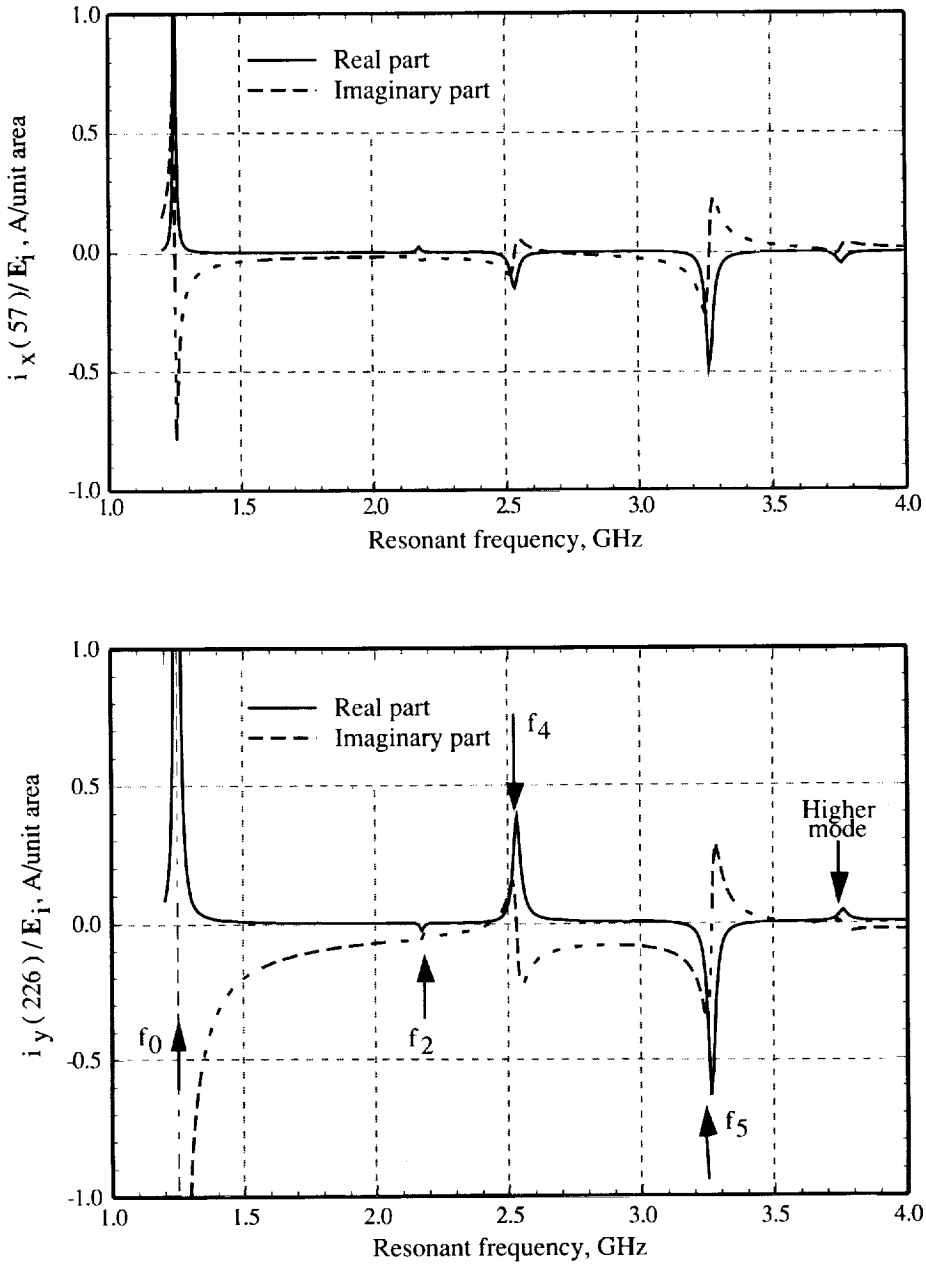

Figure 7. Normalized current density as function of resonant frequency for equilateral triangular patch (shown in fig. 2) excited by plane wave at angle of incidence of ($\theta_i = 0°$, $\phi_i = 90°$) and $M = N = 19$. The terms f_0 (1.249 GHz), f_2 (2.172 GHz), f_4 (2.525 GHz), and f_5 (3.265 GHz) are resonant frequencies of TM_{01}, TM_{11}, TM_{02}, and TM_{12} modes, respectively.

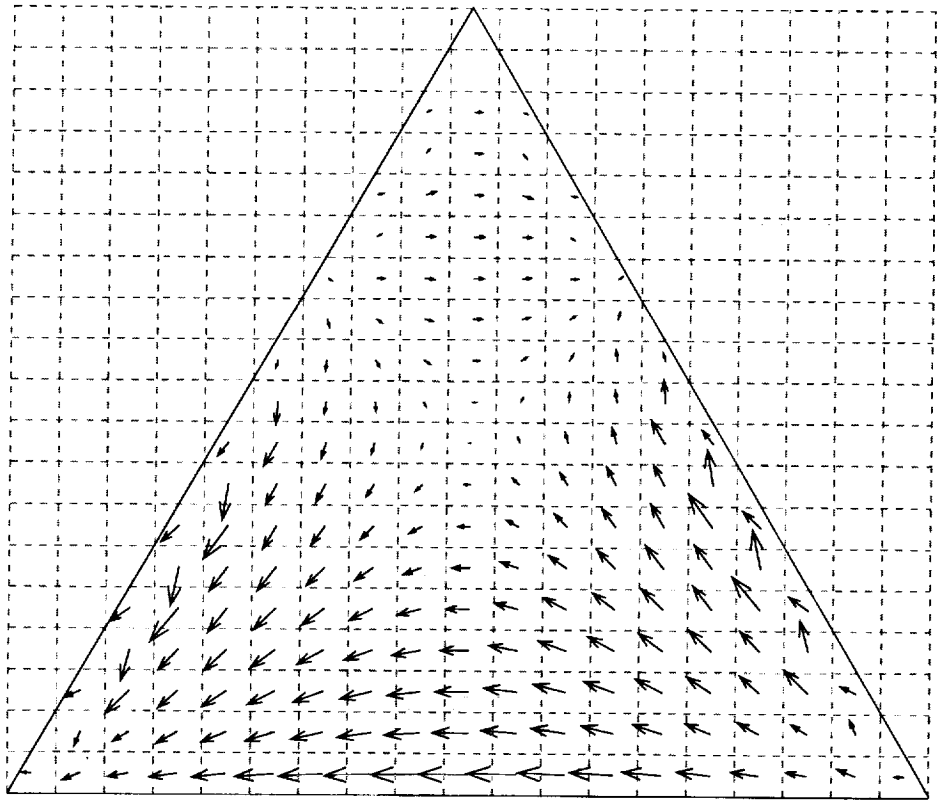

(a) $f_2 = 2.172$ GHz (TM_{11} mode case).

Figure 8. Vectorial representation of surface-current density on equilateral triangular patch (shown in fig. 2) excited by plane wave with angle of incidence of ($\theta_i = 0°$, $\phi_i = 0°$) and resonant frequencies $f_2 = 2.172$ GHz (TM_{11} mode case), $f_4 = 2.510$ GHz (TM_{20} mode case), and $f_5 = 3.355$ GHz (TM_{21} mode case).

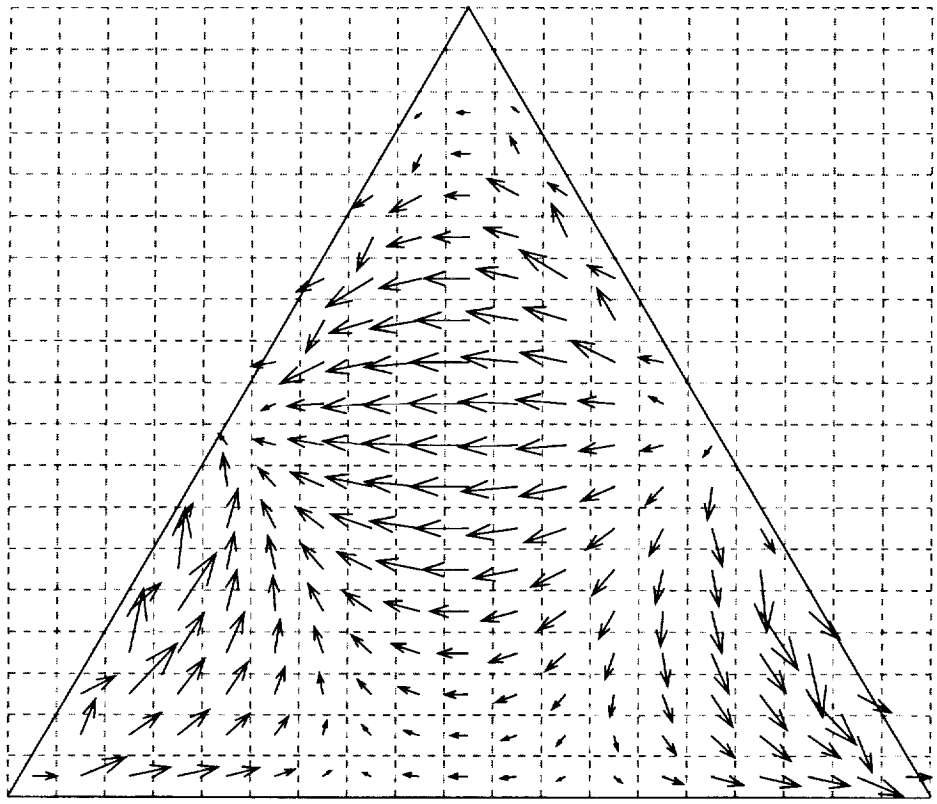

(b) $f_4 = 2.510$ GHz (TM_{20} mode case).

Figure 8. Continued.

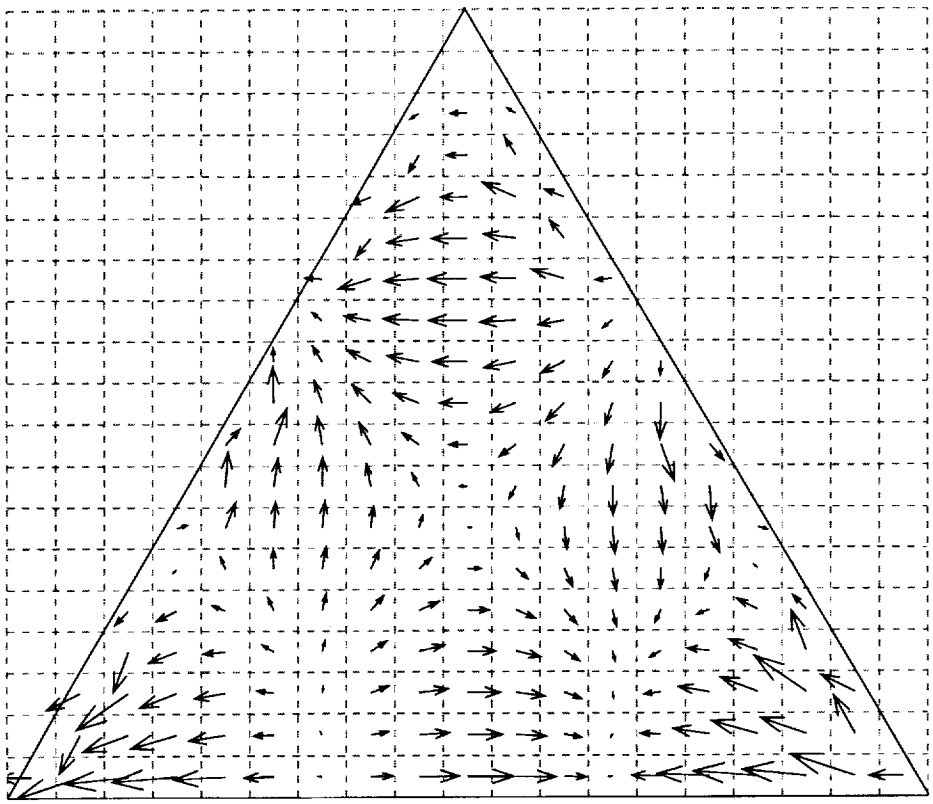

(c) $f_5 = 3.355$ GHz (TM_{21} mode case).

Figure 8. Concluded.

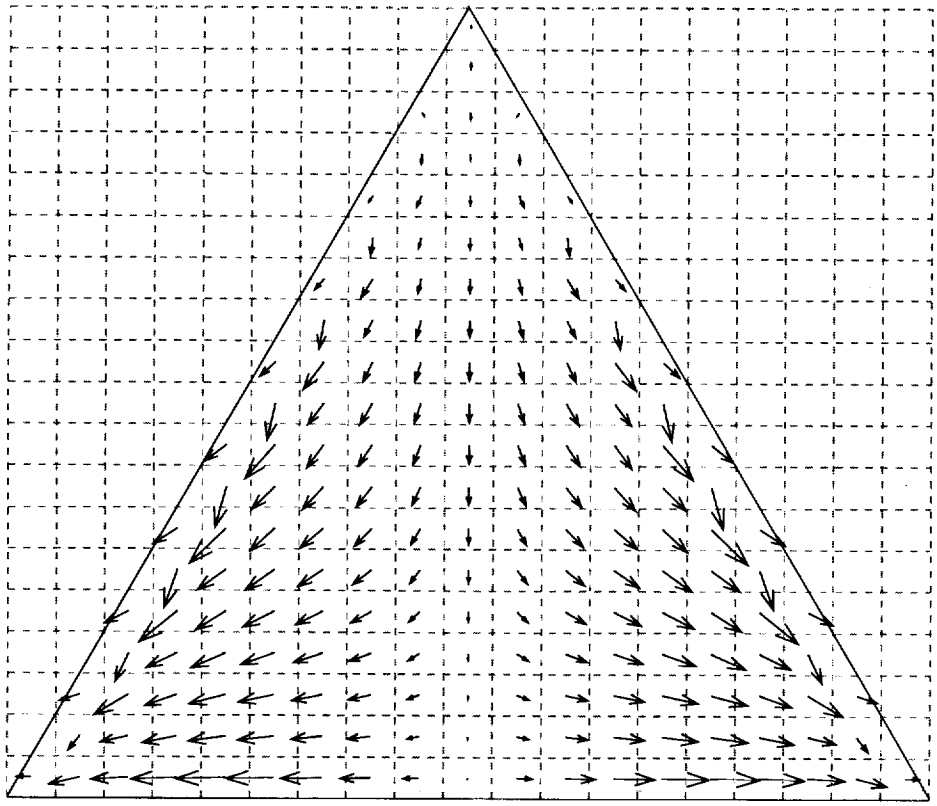

(a) $f_2 = 2.172$ GHz (TM_{11} mode case).

Figure 9. Vectorial representation of surface-current density on equilateral triangular patch (shown in fig. 2) excited by plane wave with angle of incidence of ($\theta_i = 0°$, $\phi_i = 90°$) and resonant frequencies $f_2 = 2.172$ GHz (TM_{11} mode case), $f_4 = 2.510$ GHz (TM_{02} mode case), and $f_5 = 3.265$ GHz (TM_{12} mode case).

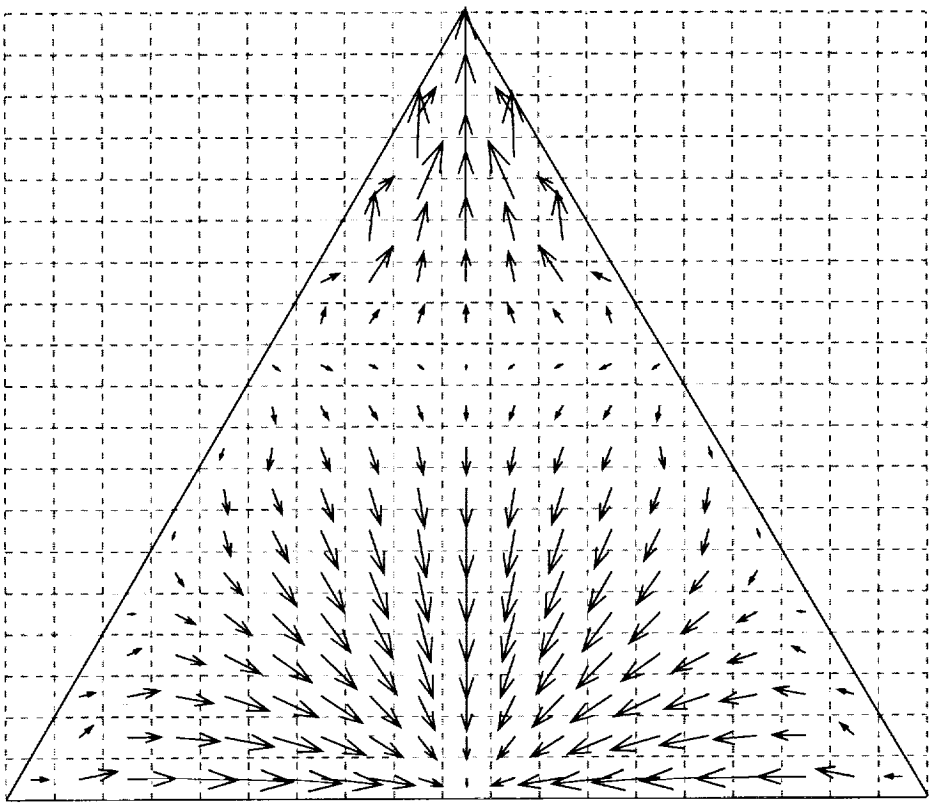

(b) $f_4 = 2.510$ GHz (TM_{02} mode case).

Figure 9. Continued.

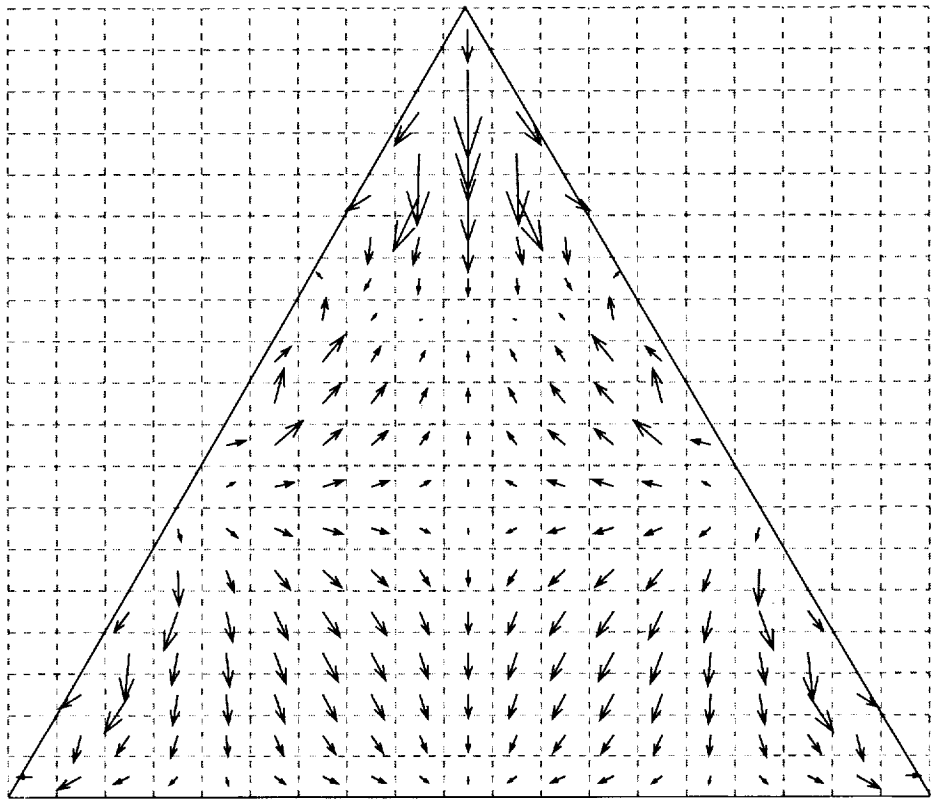

(c) $f_5 = 3.265$ GHz (TM_{12} mode case).

Figure 9. Concluded.

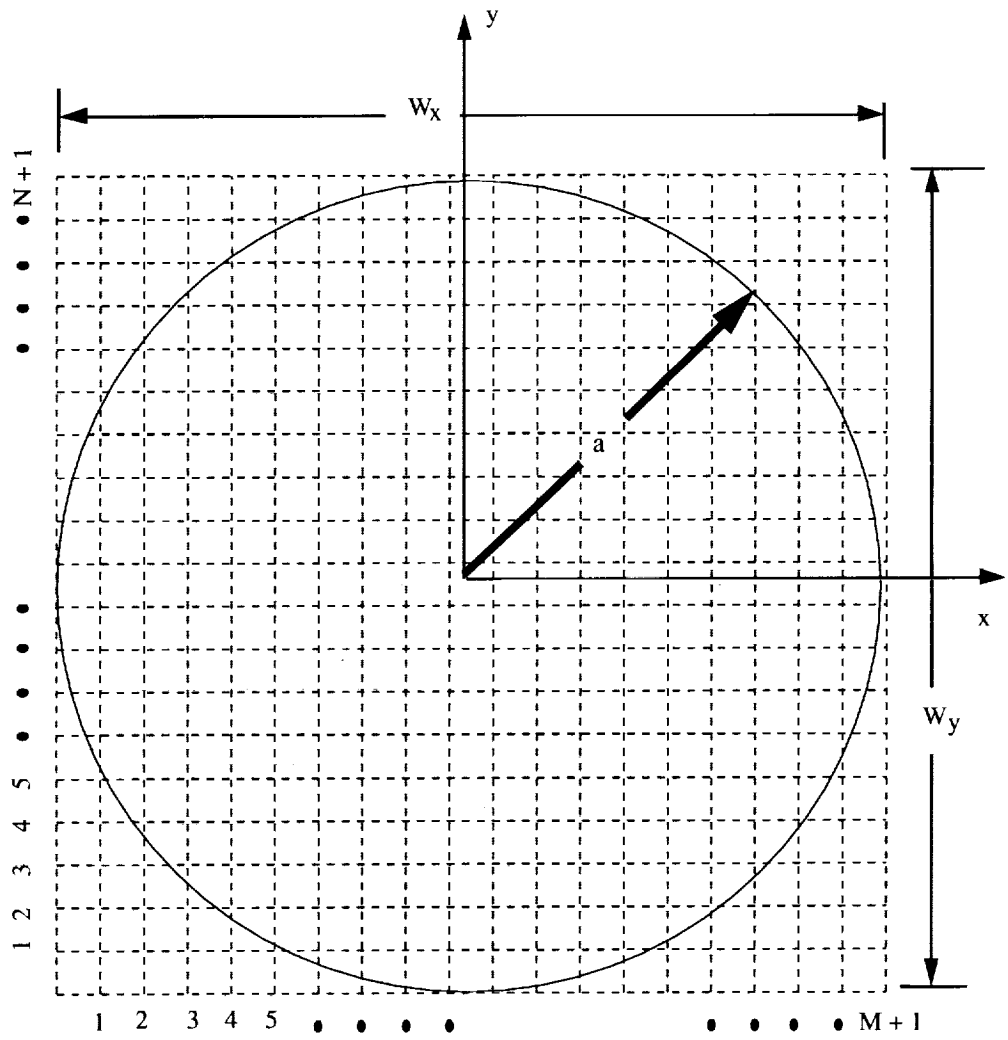

Figure 10. Geometry of circular patch with radius a = 1.88 cm, $d = z' = 0.16$ cm, $\varepsilon_r = 2.53$, and Loss tangent = 0.002.

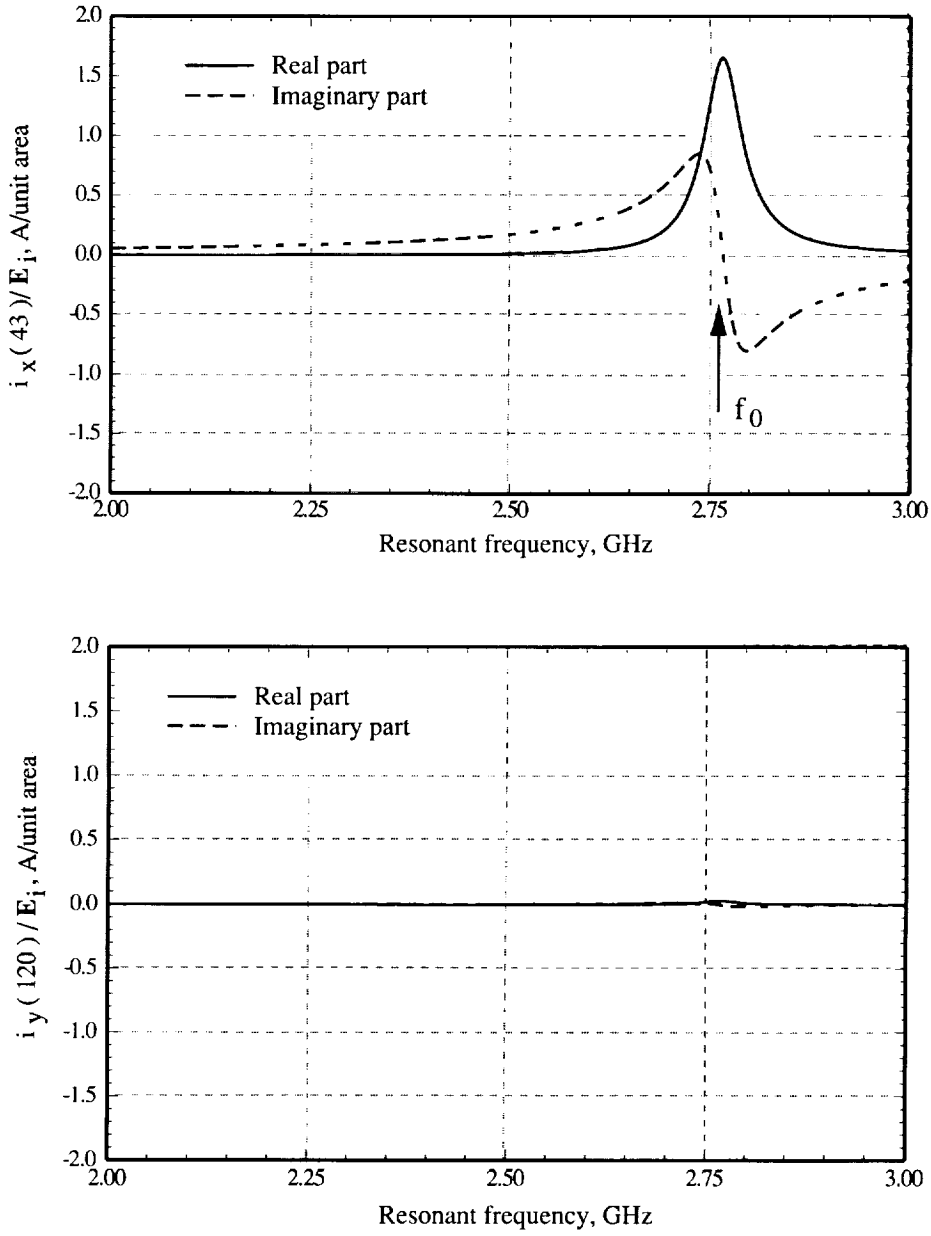

(a) $(\theta_i = 0°, \phi_i = 0°)$.

Figure 11. Normalized current density as function of resonant frequency for circular patch (shown in fig. 10) for angles of incidence of $(\theta_i = 0°, \phi_i = 0°)$ and $(\theta_i = 0°, \phi_i = 90°)$, $M = N = 11$, and $f_0 = 2.76$ GHz.

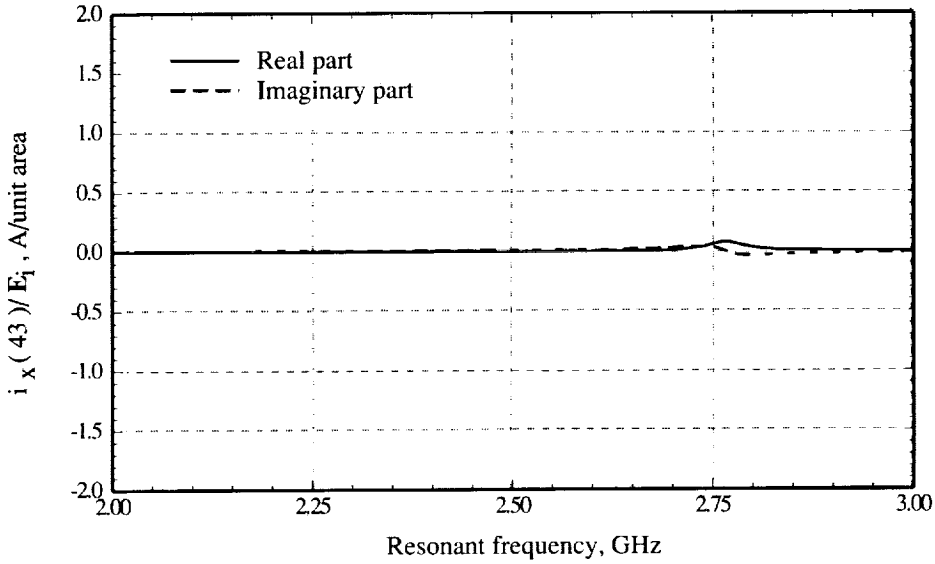

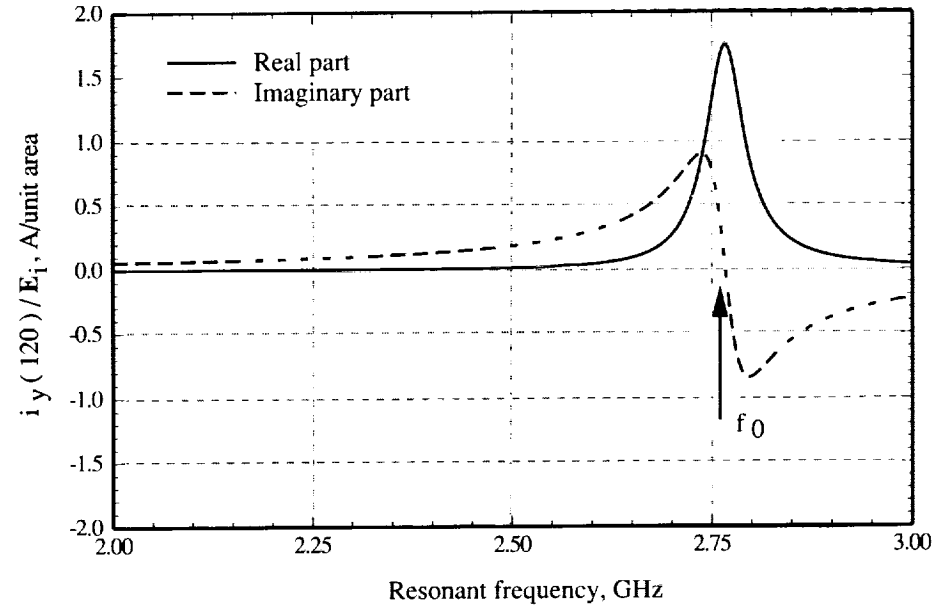

(b) $(\theta_i = 0°, \phi_i = 90°)$.

Figure 11. Concluded.

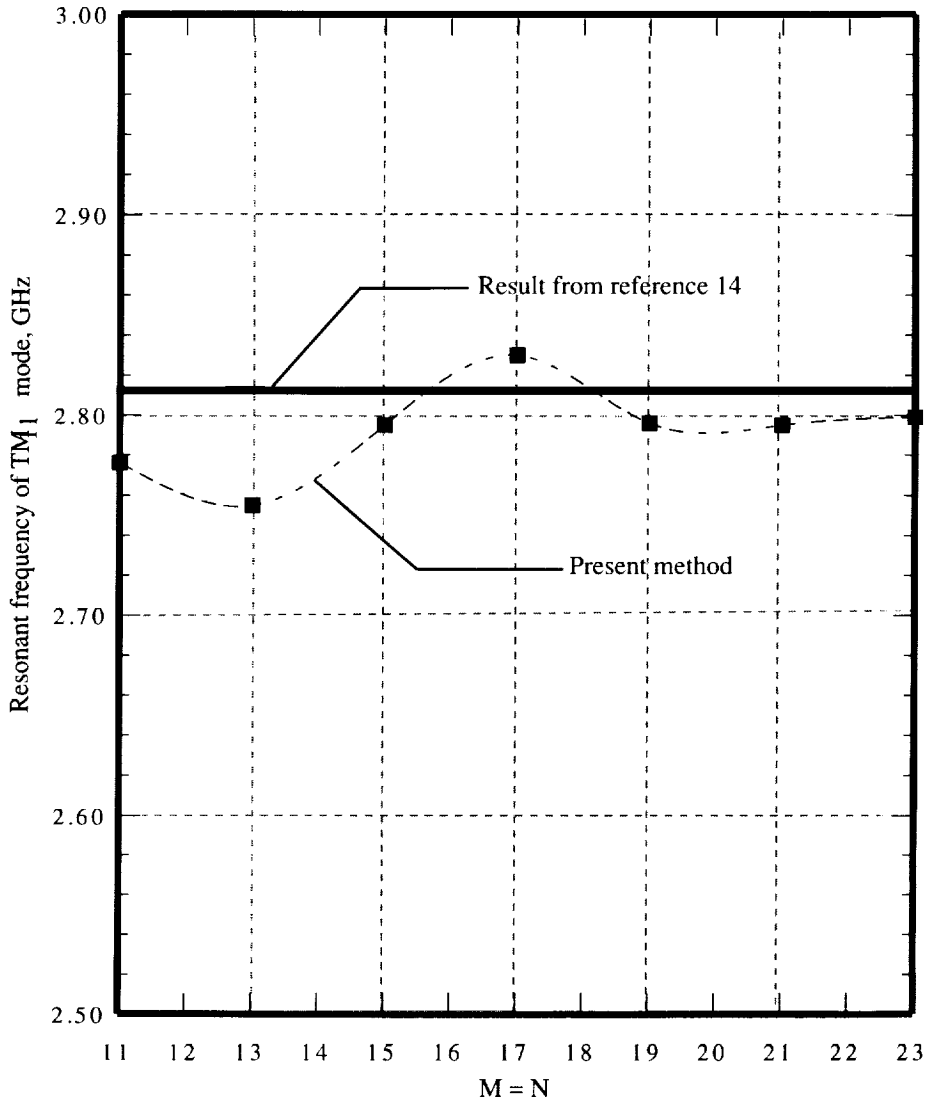

Figure 12. Resonant frequency of circular patch TM_{11} mode (shown in fig. 10), excited by plane wave at angle of incidence of ($\theta_i = 0°$, $\phi_i = 0°$) as function of $M = N$.

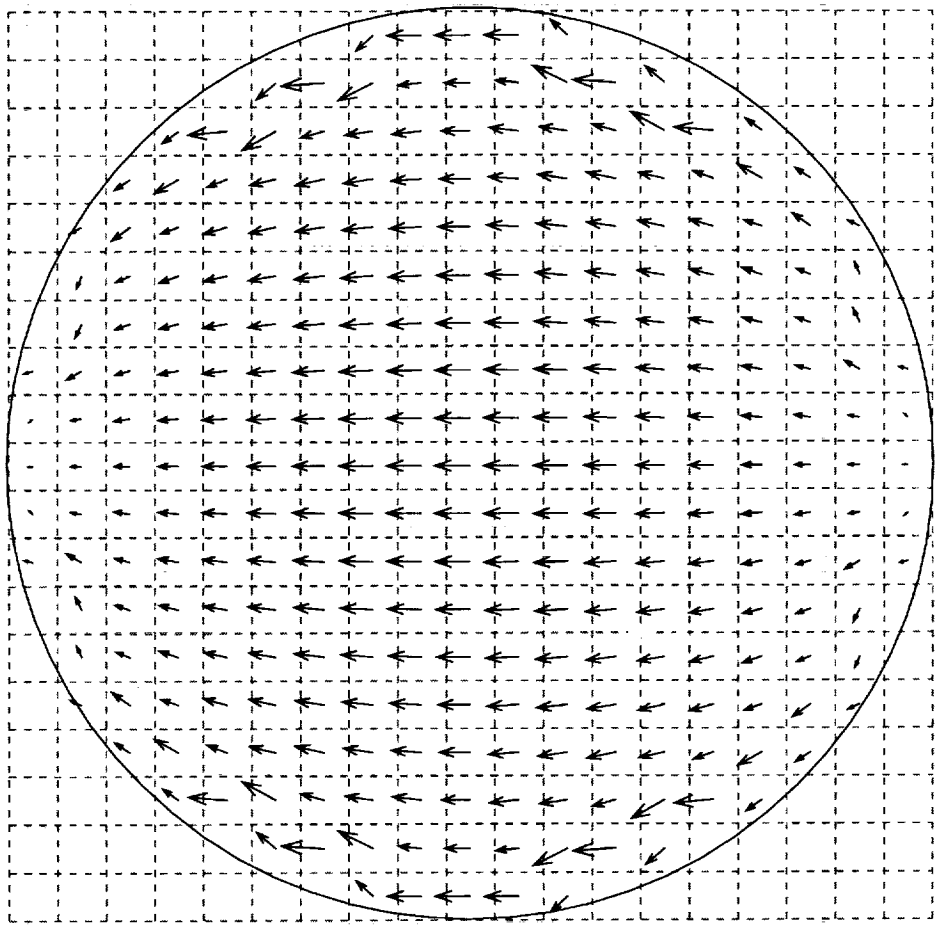

(a) $(\theta_i = 0°, \phi_i = 0°)$.

Figure 13. Vectorial representation of surface-current density on circular patch (shown in fig. 10) excited by plane wave with angles of incidence of $(\theta_i = 0°, \phi_i = 0°)$ and $(\theta_i = 0°, \phi_i = 90°)$ and $f_0 = 2.796$ GHz (TM_{11} mode case).

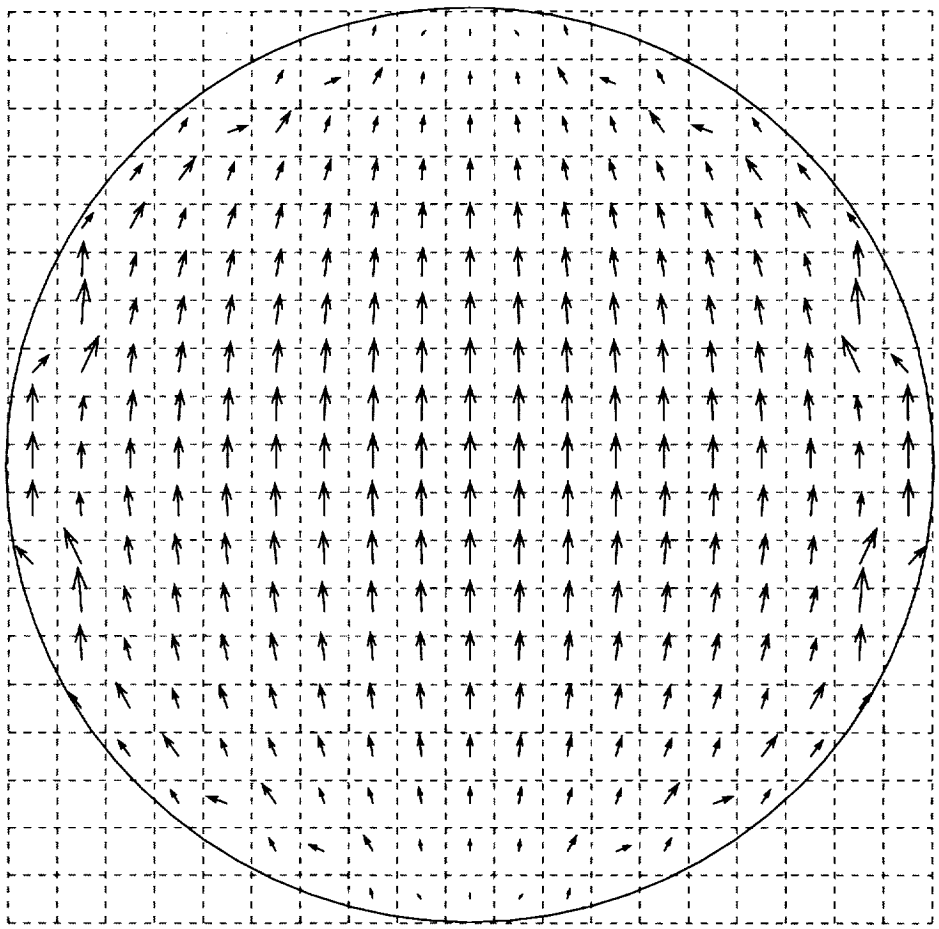

(b) ($\theta_i = 0°$, $\phi_i = 90°$).

Figure 13. Concluded.

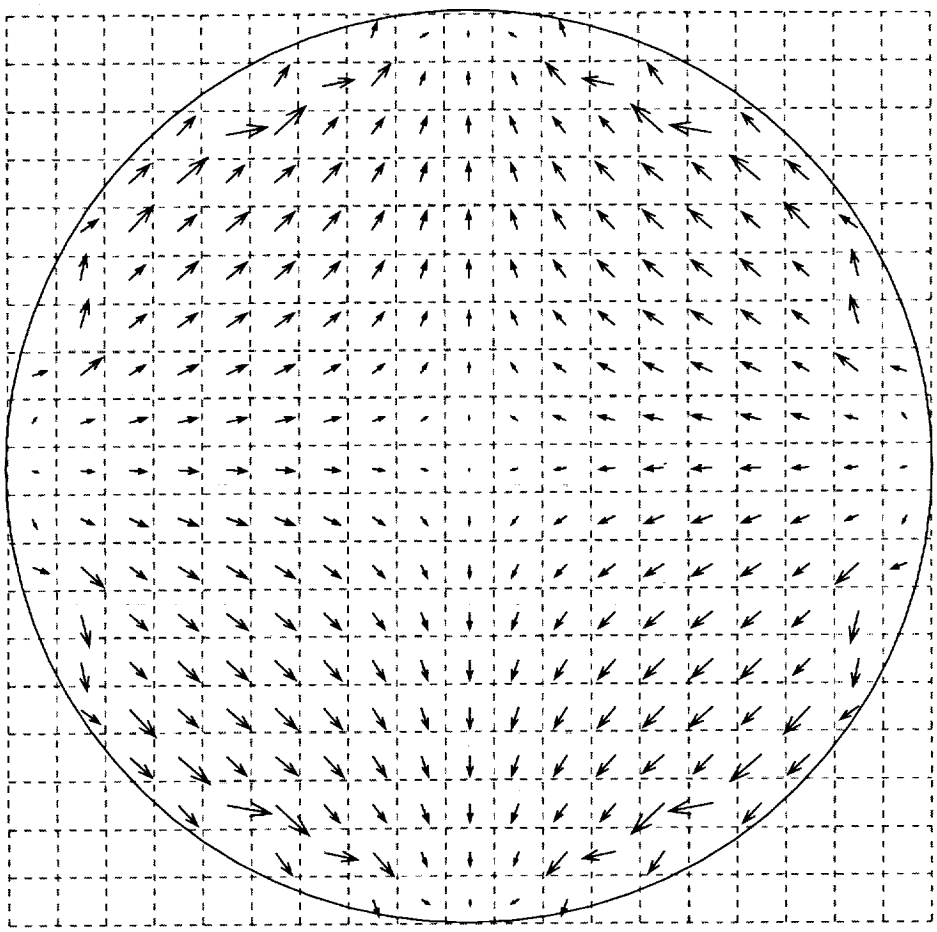

(a) $f_1 = 4.685$ GHz (TM_{21} mode case).

Figure 14. Vectorial representation of surface-current density on circular patch (shown in fig. 10) excited by plane wave with angle of incidence of ($\theta_i = 45°$, $\phi_i = 90°$) and resonant frequencies $f_1 = 4.685$ GHz (TM_{21} mode case), $f_2 = 5.855$ GHz (TM_{02} mode case), and $f_3 = 6.360$ GHz (TM_{31} mode case).

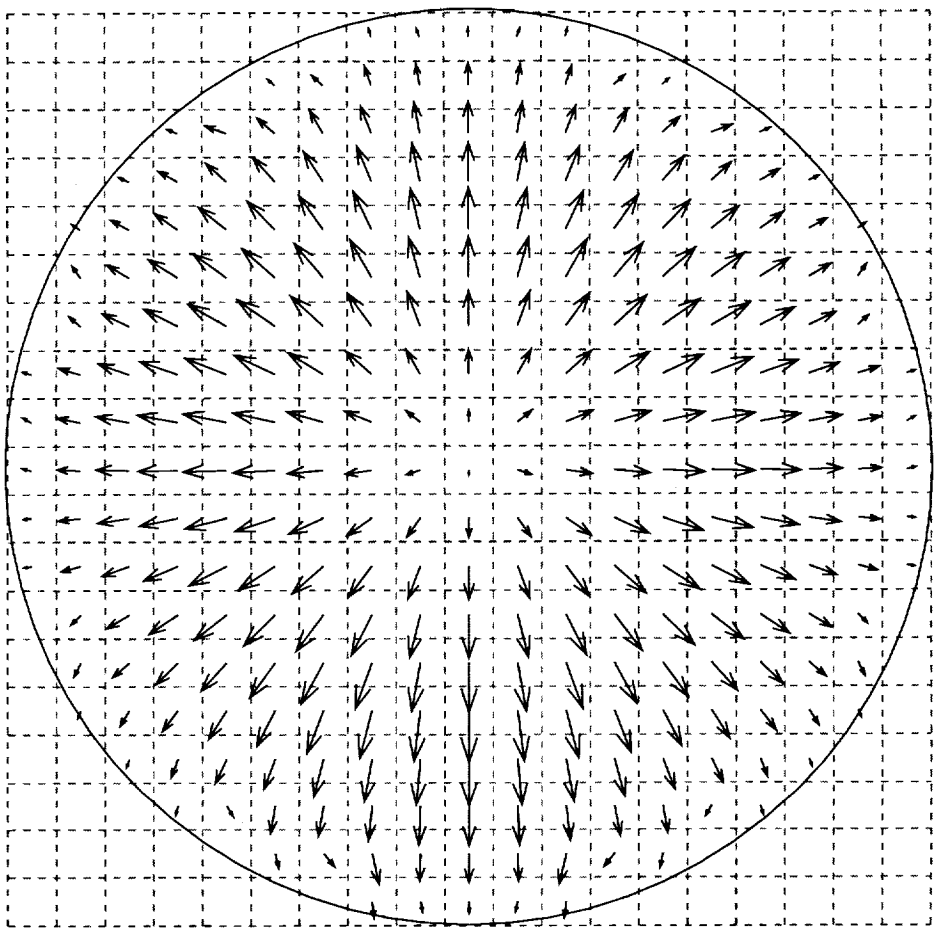

(b) $f_2 = 5.855$ GHz (TM_{02} mode case).

Figure 14. Continued.

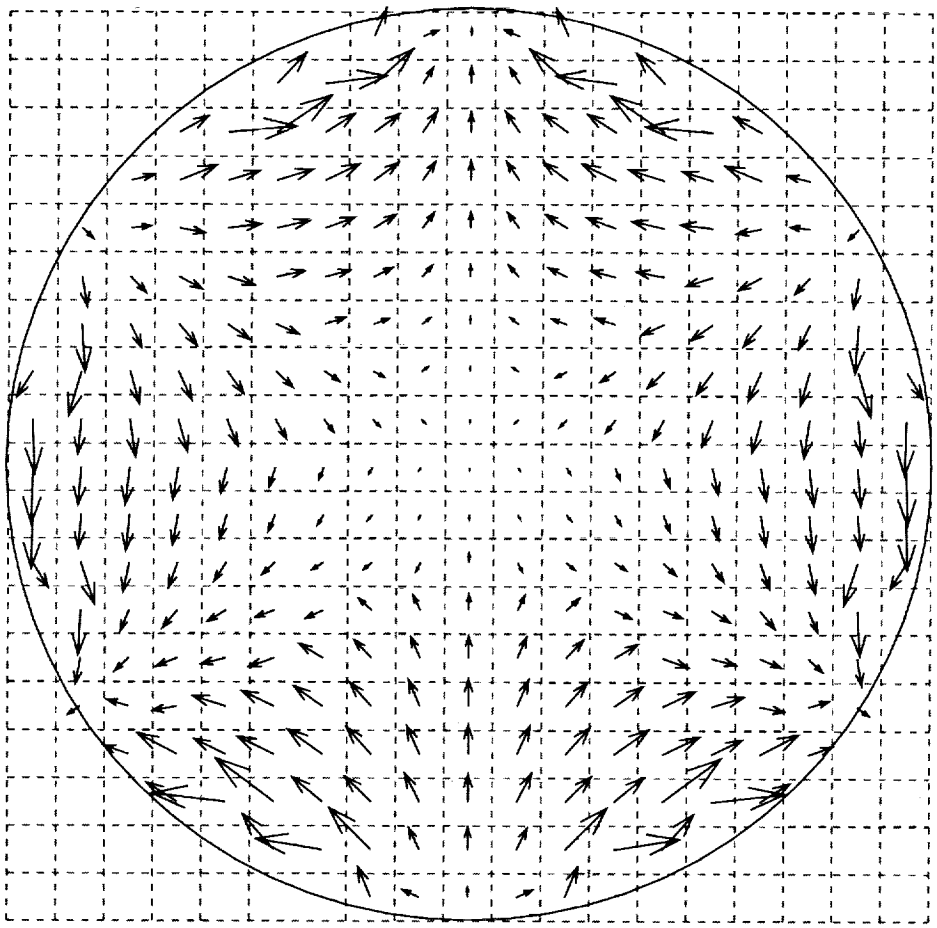

(c) $f_3 = 6.360$ GHz (TM_{31} mode case).

Figure 14. Concluded.

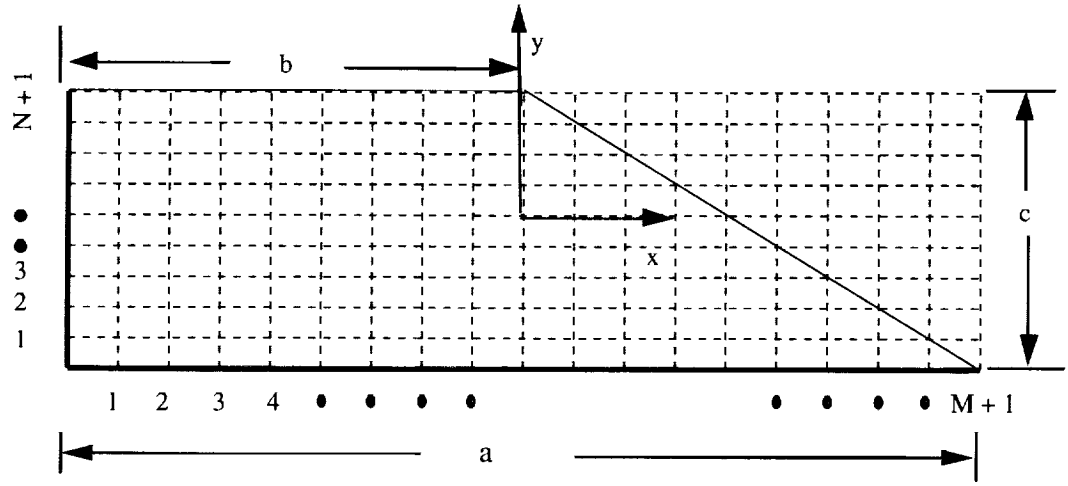

Figure 15. Geometry of trapezoidal patch with radius a = 8.08 cm, $b = c = 4.04$ cm, $d = z' = 0.16$ cm, $\alpha = 45$, $\varepsilon_r = 2.65$, and Loss tangent = 0.002.

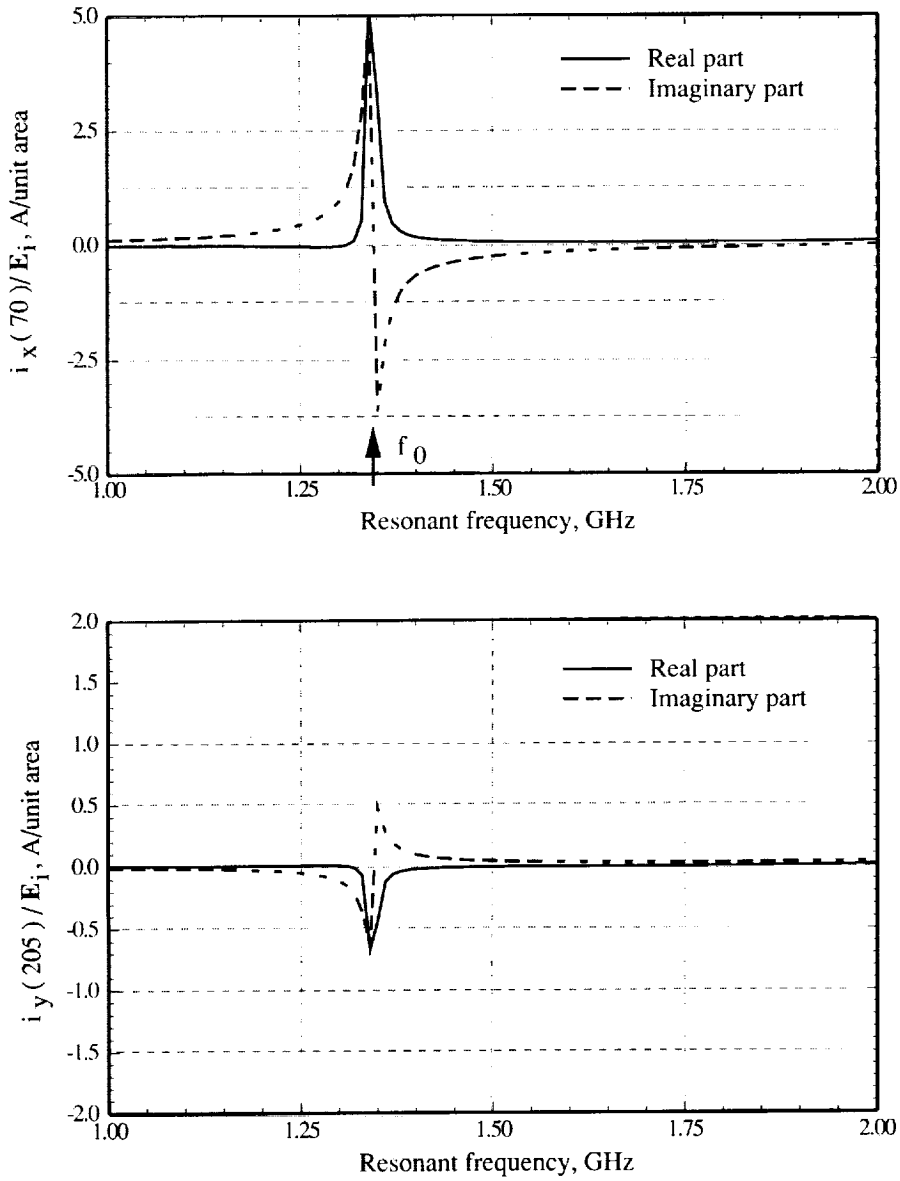

(a) $(\theta_i = 45°, \phi_i = 0°)$.

Figure 16. Normalized current density as function of resonant frequency for trapezoidal patch (shown in fig. 15) excited by plane wave at angles of incidence of $(\theta_i = 45°, \phi_i = 0°)$ and $(\theta_i = 45°, \phi_i = 90°)$, $M = 20$, and $N = 10$.

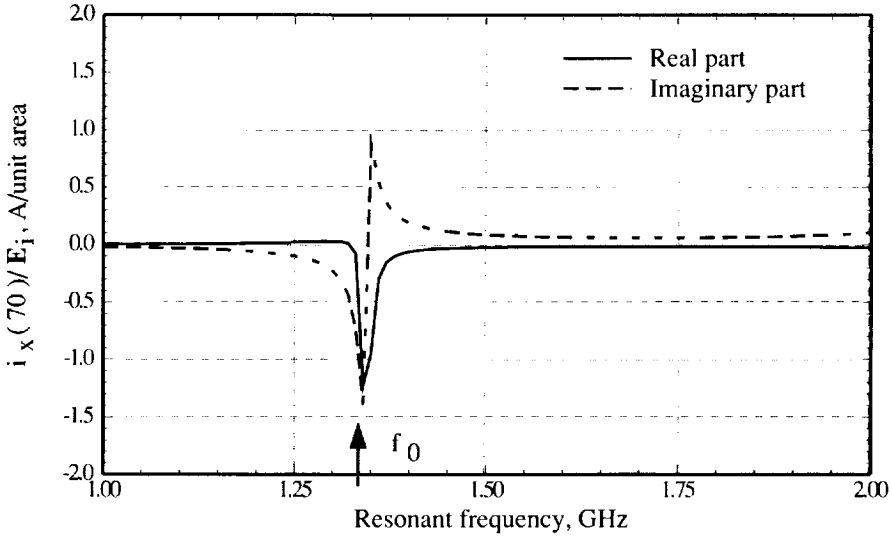

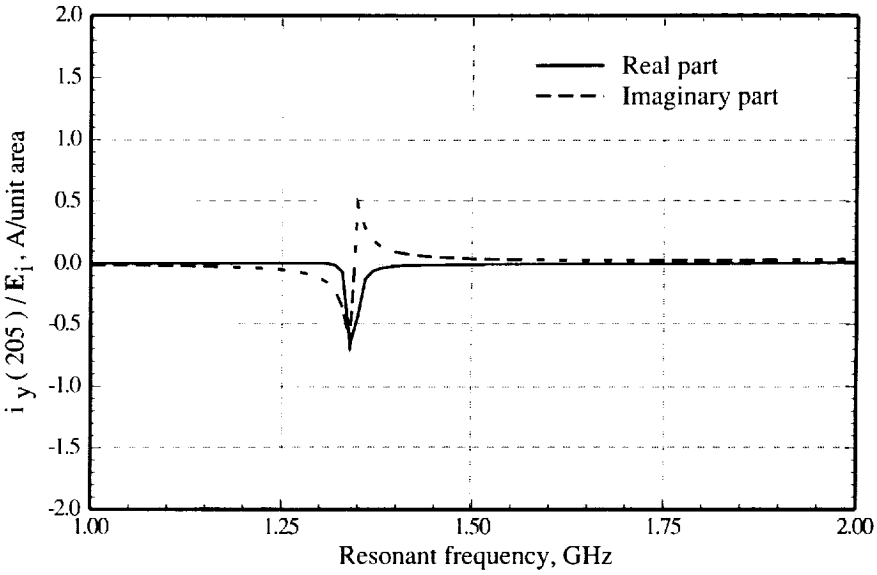

(b) ($\theta_i = 45°$, $\phi_i = 90°$).

Figure 16. Concluded.

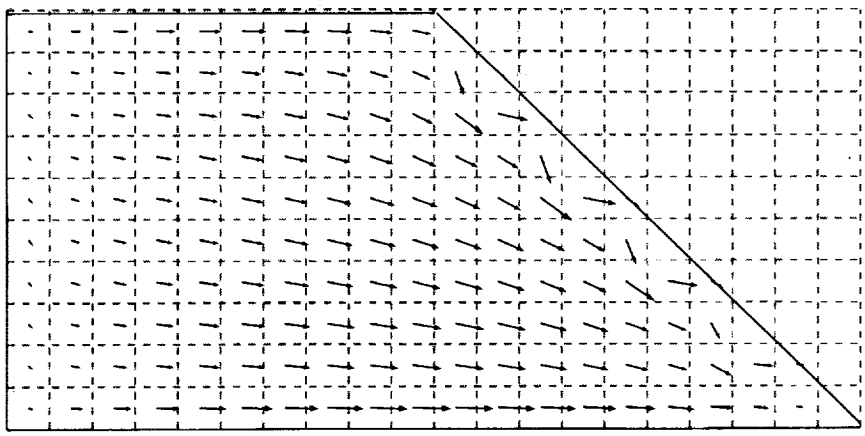

Figure 17. Vectorial representation of surface-current density on trapezoidal patch (shown in fig. 15) excited by plane wave with angle of incidence of ($\theta_i = 0°$, $\phi_i = 0°$), $f_0 = 1.345$ GHz, $M = 20$, and $N = 10$.

REPORT DOCUMENTATION PAGE

Form Approved
OMB No. 0704-0188

1. AGENCY USE ONLY *(Leave blank)*	2. REPORT DATE	3. REPORT TYPE AND DATES COVERED
	October 1993	Technical Paper

4. TITLE AND SUBTITLE
Resonant Frequencies of Irregularly Shaped Microstrip Antennas Using Method of Moments

5. FUNDING NUMBERS
WU 505-64-70-01
PR 1L162211AH85

6. AUTHOR(S)
Manohar D. Deshpande, David G. Shively, and C. R. Cockrell

7. PERFORMING ORGANIZATION NAME(S) AND ADDRESS(ES)
NASA Langley Research Center
Hampton, VA 23681-0001

Joint Research Program Office
Electronics Integration Directorate
Communications Electronics Command
Langley Research Center
Hampton, VA 23681-0001

8. PERFORMING ORGANIZATION REPORT NUMBER
L-17160

9. SPONSORING/MONITORING AGENCY NAME(S) AND ADDRESS(ES)
National Aeronautics and Space Administration
Washington, DC 20546-0001
and
U.S. Army Communications Electronics Command
Fort Monmouth, NJ 07703-5603

10. SPONSORING/MONITORING AGENCY REPORT NUMBER
NASA TP-3386
CECOM TR-93-E-1

11. SUPPLEMENTARY NOTES
Deshpande: ViGYAN, Inc., Hampton, VA; Shively: Joint Research Program Office, EID-CECOM, Langley Research Center, Hampton, VA; Cockrell: Langley Research Center, Hampton, VA.

12a. DISTRIBUTION/AVAILABILITY STATEMENT
Unclassified–Unlimited

Subject Category 32

12b. DISTRIBUTION CODE

13. ABSTRACT *(Maximum 200 words)*
This paper describes an application of the method of moments to determine resonant frequencies of irregularly shaped microstrip patches embedded in a grounded dielectric slab. For analysis, the microstrip patch is assumed to be excited by a linearly polarized plane wave that is normal to the patch. The surface-current density that is induced on the patch because of the incident field is expressed in terms of subdomain functions by dividing the patch into identical rectangular subdomains. The amplitudes of the subdomain functions, as a function of frequency, are determined using the electric-field integral equation (EFIE) approach in conjunction with the method of moments. The resonant frequencies of the patch are then obtained by selecting the frequency at which the amplitude of the surface-current density is real. The resonant frequencies of the equilateral triangular and other nonrectangular patches are computed using the present technique, and these frequencies are compared with measurements and other independent calculations.

14. SUBJECT TERMS
Antennas; Microstrip; Resonant frequency; Method of moments

15. NUMBER OF PAGES
39

16. PRICE CODE
A03

17. SECURITY CLASSIFICATION OF REPORT	18. SECURITY CLASSIFICATION OF THIS PAGE	19. SECURITY CLASSIFICATION OF ABSTRACT	20. LIMITATION OF ABSTRACT
Unclassified	Unclassified	Unclassified	

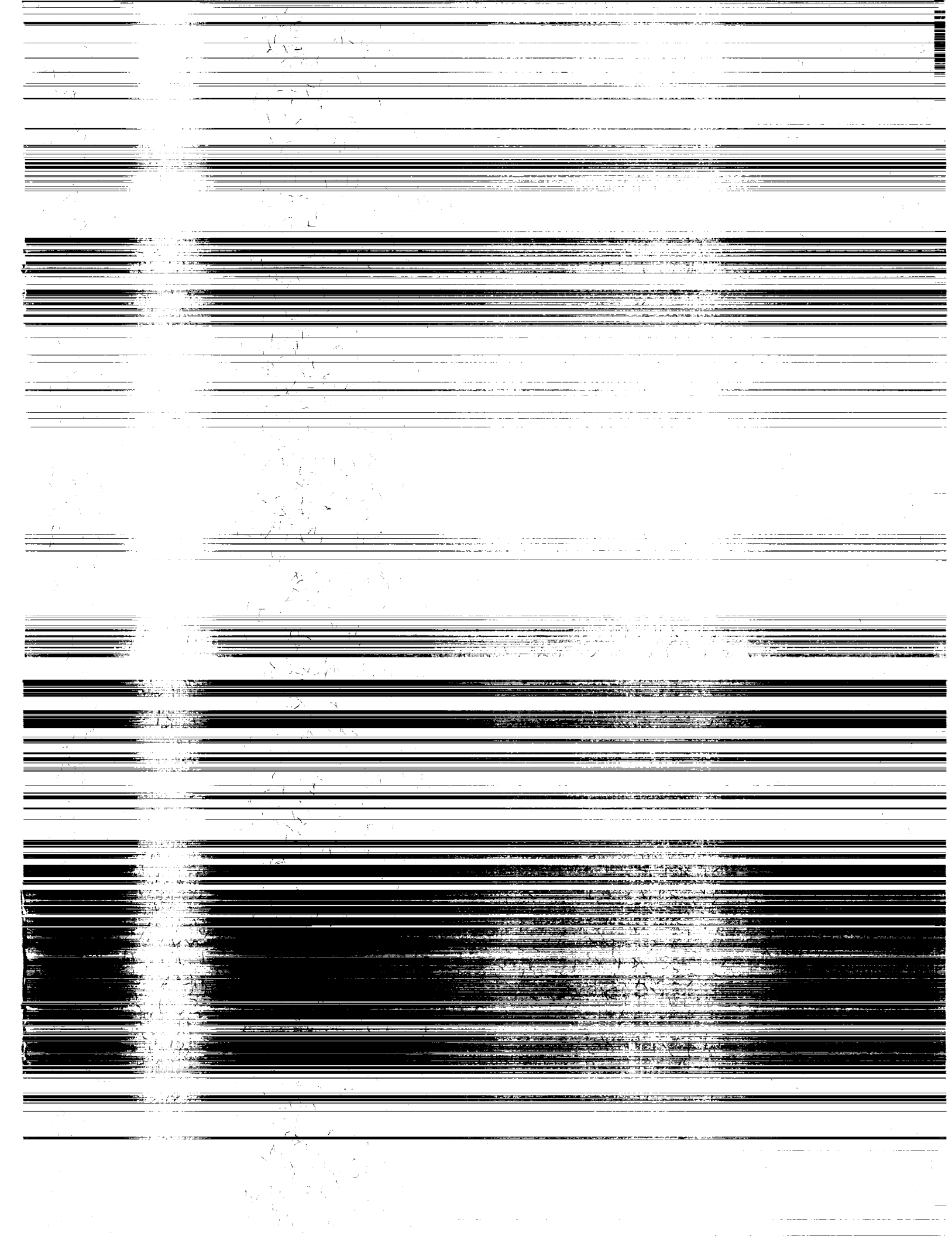

National Aeronautics and
Space Administration
Code JTT
Washington, D.C.
20546-0001

Official Business

Penalty for Private Use, $300

BULK RATE
POSTAGE & FEES PAID
NASA
Permit No. G-27

NASA

POSTMASTER: If Undeliverable (Section 158 Postal Manual) Do Not Return